A unifying computational fluid dynamics investigation on the river-like to river-reversed secondary circulation in submarine channel bends

F. Giorgio Serchi,[1,2] J. Peakall,[2] D. B. Ingham,[1] and A. D. Burns[1]

Received 20 April 2010; revised 17 February 2011; accepted 22 March 2011; published 18 June 2011.

[1] A numerical model of saline density currents across a triple-bend sinuous submerged channel enclosed by vertical sidewalls is developed. The unsteady, non-Boussinesq, turbulent form of the Reynolds Averaged Navier-Stokes equations is employed to study the flow structure in a quasi-steady state. Recursive tests are performed with axial slopes of 0.08°, 0.43°, 1.5°, and 2.5°. For each numerical experiment, the downstream and vertical components of the fluid velocity, density, and turbulent kinetic energy are presented at four distinct locations within the channel cross section. It is observed that a crucial change in the flow pattern at the channel bends is observed as the axial slope is increased. At low values of the axial slope a typical river-like pattern is found. At an inclination of 1.5°a transition starts to occur. When the numerical test is repeated with an axial slope of 2.5°, a clearly visible river-reversed secondary circulation is achieved. The change in the cross-sectional flow pattern appears to be associated with the spatial displacement of the core of the maximum downstream fluid velocity. Therefore, the axial slope in this series of experiments is linked to the velocity structure of the currents, with the height of the velocity maximum decreasing as a function of increasing slope. As such, the axial slope should be regarded also as a surrogate for flows with enhanced density or sediment stratification and higher Froude numbers. The work unifies the apparently paradoxical experimental and numerical results on secondary circulation in submarine channels.

Citation: Giorgio Serchi, F., J. Peakall, D. B. Ingham, and A. D. Burns (2011), A unifying computational fluid dynamics investigation on the river-like to river-reversed secondary circulation in submarine channel bends, *J. Geophys. Res.*, *116*, C06012, doi:10.1029/2010JC006361.

1. Introduction

1.1. Rationale

[2] Submarine channels are outstanding geomorphological systems which traverse the ocean floors across the planet. They may extend for thousands of kilometers [*Chough and Hesse*, 1980] and act as the primary conduits for massive amounts of sediment [*Middleton*, 1993]. The clastic material supplied by the shelf and slope [*Hampton*, 1972; *Mohrig and Marr*, 2003] travels through such pathways producing erosive and levee-bounded sinuous channels [*Clark and Pickering*, 1996; *Peakall et al.*, 2000; *Wynn et al.*, 2007]. The transport of particulate material from the continental shelf to the deepest reaches of the ocean basins is ascribed to the various forms of density driven flows which occur in this context, these include slumps, slides and most of all turbidity currents [*Mulder and Alexander*, 2001]. Despite the crucial importance of submarine fan systems as valuable areas of exploitation for the oil industry, the understanding of the dynamics and evolution of these geomorphological features remains limited [*Peakall et al.*, 2000; *Kolla et al.*, 2007; *Wynn et al.*, 2007; *Kane et al.*, 2008]. The analogy between submarine and fluvial systems has thus been long employed, in the absence of more directly applicable theories, given their morphological similarities [*Klaucke and Hesse*, 1996; *Clark et al.*, 1992; *Imran et al.*, 1999]. However, well established discrepancies are found from the comparison of rivers with their submarine counterpart, highlighting the occurrence of different depositional processes in the two environments [*Peakall et al.*, 2000; *Kolla et al.*, 2007; *Wynn et al.*, 2007]. The mechanics which account for the development of submarine channels and which explain the complex patterns of sedimentation within the channel, on the levees and in the overbank regions, remains a topic of active investigation. Conceptual models exist based on observations from seismic exploration and outcrops [*Peakall et al.*, 2000; *Wynn et al.*, 2007], but the link with the actual flow dynamics occurring in submarine channels still remains unclear. Regardless of the technology available, the feasibility of an accurate description of such systems and the processes therein is constrained by the spatial extent and poor accessibility of submarine channels and by the difficulty in physically observing natural turbidity currents [*Zeng et al.*, 1991; *Khripounoff et al.*,

[1]School of Process Material and Environmental Engineering, CFD Centre, University of Leeds, Leeds, UK.
[2]School of Earth and Environment, Department of Earth Sciences, University of Leeds, Leeds, UK.

0148-0227/11/2010JC006361

2003; *Paull et al.*, 2003; *Xu et al.*, 2004; *Best et al.*, 2005; *Vangriesheim et al.*, 2009; *Parsons et al.*, 2010], given their extremely destructive nature. Despite providing an invaluable insight into the quantitative description of certain flow parameters, these data often lack the spatial resolution required to fully comprehend the fluid dynamics typical of submarine channel systems. An unprecedented degree of accuracy has been lately delivered by the parallel employment of laboratory-scale physical modeling and numerical models [*Imran et al.*, 2004; *Kassem and Imran*, 2004; *Keevil et al.*, 2006; *Corney et al.*, 2006; *Keevil et al.*, 2007; *Peakall et al.*, 2007a]. However, the results of the three-dimensional flow field within channels, and in particular the secondary circulation, have been apparently contradictory, producing both river-like and river-reversed secondary flow cell orientations [*Kassem and Imran*, 2004; *Corney et al.*, 2006; *Keevil et al.*, 2006, 2007; *Islam and Imran*, 2008]. While an answer to this paradox has been proposed based on an analytical model [*Corney et al.*, 2006, 2008], this model has been strongly criticized as overly simplistic and applied to flows outside of the limits of the analytical solutions [*Imran et al.*, 2007; *Islam and Imran*, 2008]. Furthermore, the model of *Corney et al.* [2006, 2008] assumes isotropic density fields, in contrast to the saline fluids utilized in the experimental programmes, and previous computational fluid dynamics (CFD) simulations.

[3] Extensive investigation exists, in contrast, on the role of stratification in curved system in the frame of tidal processes within estuaries [*Geyer*, 1993; *Chant and Wilson*, 1997; *Seim and Gregg*, 1997; *Lacy and Monismith*, 2001; *Chant*, 2002; *Cheng et al.*, 2009; *Nidzieko et al.*, 2009], which has, so far, been largely disregarded in the debate on the secondary circulation of submarine channels. Here we address the limitations in previous numerical models, through the application of a RANS based CFD model, and apply this approach to examine the enigmatic experimental and numerical results for secondary flow in submarine channels by incorporating the established understanding from estuarine systems.

1.2. Background: Secondary Circulation in Density-Driven Estuarine Flows

[4] The onset of a secondary circulation in channelized systems is not unique to submarine channels. The cross channel flow processes in estuarine systems have been long studied both by means of numerical models [*Cheng et al.*, 2009] and observational field analysis [*Geyer*, 1993; *Chant and Wilson*, 1997; *Seim and Gregg*, 1997; *Lacy and Monismith*, 2001; *Chant*, 2002; *Nidzieko et al.*, 2009]. The secondary circulation most commonly found in estuaries closely resembles that of open channel systems [*Geyer*, 1993; *Seim and Gregg*, 1997], where the basal and surface flows are directed toward the inner and outer sides of the bend, respectively. However, secondary circulation both with a reversed sense of rotation [*Chant and Wilson*, 1997; *Seim and Gregg*, 1997; *Lacy and Monismith*, 2001; *Nidzieko et al.*, 2009] and with multicelled structure [*Cheng et al.*, 2009; *Nidzieko et al.*, 2009] is not uncommon and has been recorded in several examples. There is evidence that the onset of a reversed cross channel circulation in estuaries is driven by the interplay of terms which include curvature, Coriolis force, structure of the streamwise flow, rate of turbulence exchange and structure of the longitudinal and transverse density gradients. The relative importance of these terms provides the key point for interpreting the driving mechanism of one mode of circulation rather than the other. While the Coriolis forcing is sometimes regarded as a less influential term in determining the local pattern of secondary circulation, curvature and stratification are, instead, recognized as being of primary importance. These two terms are especially relevant to the case of submarine channel. Curvature is responsible for producing centrifugal accelerations which are always directed toward the outer side of a bend and are often predominant over the other terms. The effect of stratification upon the flow is largely non linear, however two possible scenarios are envisaged:

[5] 1. Sharp vertical density gradients in the channel cross section give rise to a strongly stratified fluid. The enhanced stratification of a tidal flow supports the onset of intense vertical shear, which in turn dampens the vertical cross channel viscosity. As a result of this, the streamwise flow is allowed to travel faster as well as being subject to an increased centrifugal acceleration. This interaction between the stratification and the transverse centrifugal term was employed by *Geyer* [1993] to explain the unexpectedly high cross-sectional velocities during the tidal cycle at Gay Head, Massachusetts.

[6] 2. Tilted isopycnals in a channel cross section are responsible for generating remarkable baroclinic pressure gradients, which can grow as large as the centrifugal term. The baroclinic circulation is usually directed toward the inside of a bend, thus opposing the centrifugal acceleration. This has been observed to lead to either weakening or even annihilation of the secondary circulation [*Chant and Wilson*, 1997; *Seim and Gregg*, 1997] and to the formation of a flow cell where the basal flow travels toward the outer side of the channel and the surface flow travels toward the inner side [*Lacy and Monismith*, 2001; *Nidzieko et al.*, 2009].

[7] These assumptions are retained as the key points for investigating the dynamics of underflows in curved, submerged channels.

1.3. Background: Secondary Circulation in Submarine Channels

[8] In the context of submarine channels, the first detailed analysis of the secondary circulation which accounts for the full fluid dynamics of the problem, at least for the case of solute-driven flows, is that from *Kassem and Imran* [2004]. Here unsteady turbulent saline flows are modeled in a series of different geometrical configurations, including a sinuous-shaped channel, until quasi-steady state is reached. *Kassem and Imran* [2004] supported the hypothesis that secondary circulation at submarine channel bends resembles that of subaerial meandering systems. In their simulation of a saline flow in a submerged sinuous channel, *Kassem and Imran* [2004] observed a major basal component from the outer to the inner bank at the channel bends along with a proportional backflow from the inner to the outer bank located at approximately the levee height. These results were questioned when the first set of laboratory measurements from a physical model of a saline density current flowing across a submerged meandering channel were presented [*Keevil et al.*, 2006]. The data set unequivocally contradicted the numerical results of *Kassem and Imran* [2004], revealing the onset of a secondary circulation at the channel bends reversed to that of

subaerial channels. The secondary flow patterns from *Keevil et al.* [2006] show basal flow directed from the inner to the outer bank and a backflow from the outer to the inner bank placed at the levee height. The reversed secondary circulation was regarded as a key factor which could possibly justify the discrepancies in morphological terms between submarine and subaerial channels. An adaptation to the submerged case of the analytical model of *Kikkawa et al.* [1976] for secondary flow at river bends was developed by *Corney et al.* [2006] confirming the recent outcome of *Keevil et al.* [2006]. This was followed by a further experimental analysis [*Keevil et al.*, 2007] that examined channels with different axial slope, width to depth ratios, cross-sectional shape, overbank topography and scale of the entire experimental apparatus. The occurrence of a river-reversed flow pattern at the channel bends was systematically observed in every experiment, thus casting further uncertainty on the causes of the mismatch with the outcomes of the numerical studies of *Kassem and Imran* [2004]. A second experimental program on a single bend submerged channel with saline gravity currents demonstrated that a river-like secondary flow analogous to that predicted by the numerical model of *Kassem and Imran* [2004] could be physically observed in the laboratory [*Imran et al.*, 2007; *Islam and Imran*, 2008]. In response to the criticism concerning the dubious reliability of the CFD model of *Kassem and Imran* [2004] due to its low degree of resolution, new experimental observations were presented by *Imran et al.* [2007] together with a refined, mesh-independent set of numerical results. Here the grid-converged solutions produced by the CFD model of the single bend submerged channel of *Islam and Imran* [2008] showed a good fit with the experimental measurements and an overall qualitative agreement with the previous numerical results of *Kassem and Imran* [2004]. Furthermore, criticism were made of the analytical model of *Corney et al.* [2006] which stretched its own underlying assumptions and was considered overly simplified [*Imran et al.*, 2008]. Finally a reply to *Imran et al.* [2008] was given by *Corney et al.* [2008] where the validity of the original model of *Corney et al.* [2006] was further motivated and expansion of the earlier results was provided. In the work of *Corney et al.* [2008] the transition from the river-like to river-reversed secondary circulation was suggested to be correlated to the different height above the channel bed of the point of maximum downstream velocity. The outcome discussed by *Corney et al.* [2008], based on a very crude approximation which fails outside very stringent assumptions, remains so far supported by theoretical analysis alone, since a transition from "river-like" to "river-reversed" flow type has never been physically observed [see *Keevil et al.*, 2007] in submarine channels. In this paper a CFD numerical model similar to that utilized by *Imran et al.* [2004] is employed. The model is revisited in order to account for a more accurate near-wall mathematical treatment of the channel bed layer and the numerical predictions are evaluated on the basis of the well established experience on stratified flows derived from estuarine systems.

2. Governing Equations

2.1. Favre-Averaged RANS Model

[9] The numerical model is developed using the commercial software FLUENT 6.3. A mixture of salt water is released from the channel inflow into fresh water, which represents the ambient fluid. The reduced gravity is given by $g' = g\frac{(\rho_1-\rho_0)}{\rho_0}$, where ρ_0 is the density of the ambient fluid, ρ_1 is the density of the heavier fluid and $g = 9.81\ \mathrm{m\ s^{-2}}$ is the magnitude of the gravitational acceleration. The flow is fully turbulent and isothermal, with density changing in space and time due to the displacement of the saline density current. The Favre averaged form of the compressible, unsteady, three-dimensional Navier-Stokes equation is solved herein. The RANS RNG $k-\epsilon$ model was employed in line with earlier works [*Zhang et al.*, 2001; *Imran et al.*, 2004; *Corney*, 2005]. Relevant boundary effects expected to occur in the vicinity of the channel bed and channel levees were dealt with by means of the "enhanced wall treatment" formulated on the basis of the work of *Wolfstein* [1969], *Kader* [1981] and *Chen and Patel* [1988], which is reviewed in the following section. The Favre averaged, compressible RANS RNG $k-\epsilon$ model is formulated through the following set of equations where U_i, ρ, p and g_i represent the averaged components of the velocity vector, the density, the pressure and the components of the gravity vector.

$$\frac{\partial \rho}{\partial t} + \frac{\partial \rho U_i}{\partial x_i} = 0 \tag{1}$$

$$\frac{\partial \rho U_i}{\partial t} + \frac{\partial \rho U_i U_j}{\partial x_j} = \frac{\partial p}{\partial x_i} + \frac{\partial}{\partial x_i}\left(\sigma_{ij} + \tau_{ij}\right) - \rho g_i, \tag{2}$$

with

$$\sigma_{ij} = \mu\left(\frac{\partial U_i}{\partial x_j} + \frac{\partial U_j}{\partial x_i} - \frac{2}{3}\delta_{ij}\frac{\partial U_k}{\partial x_k}\right), \tag{3}$$

$$\tau_{ij} = -\frac{2}{3}\delta_{ij}k + \mu_t\left(\frac{\partial U_i}{\partial x_j} + \frac{\partial U_j}{\partial x_i} - \frac{2}{3}\delta_{ij}\frac{\partial U_k}{\partial x_k}\right), \tag{4}$$

where σ_{ij} and τ_{ij} represent the molecular and turbulent shear stresses and μ and μ_t the molecular and turbulent viscosity. The latter is defined by

$$\mu_t = \rho C_\mu \frac{k^2}{\epsilon} \tag{5}$$

with $C_\mu = 0.09$.

[10] The turbulent viscosity is expressed as a function of k and ϵ which constitute the turbulent kinetic energy and the dissipation of turbulent kinetic energy, respectively, according to the following:

$$\rho\frac{\partial k}{\partial t} + \rho U_i\frac{\partial k}{\partial x_i} = \frac{\partial}{\partial x_j}\left(\alpha_k \mu_t \frac{\partial k}{\partial x_j}\right) + G_k + G_b - \rho\epsilon \tag{6}$$

$$\rho\frac{\partial \epsilon}{\partial t} + \rho U_i\frac{\partial \epsilon}{\partial x_i} = \frac{\partial}{\partial x_j}\left(\alpha_\epsilon \mu_t \frac{\partial \epsilon}{\partial x_j}\right) + C_{1\epsilon}\frac{\epsilon}{k}(G_k + C_{3\epsilon}G_b) - C_{2\epsilon}\rho\frac{\epsilon^2}{k} - R_\epsilon, \tag{7}$$

where $C_{\epsilon 1} = 1.42$ and $C_{\epsilon 2} = 1.68$. Here the term G_k represents the production of turbulent kinetic energy as a result of the strain arising within the flow. The modeled form is $G_k =$

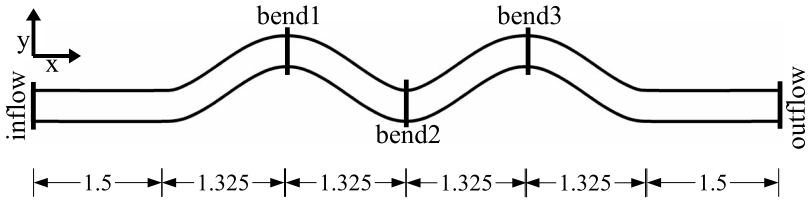

Figure 1. Channel planform adopted in this investigation in analogy with *Kassem and Imran* [2004].

$\mu_t S$, with S being the mean strain rate $S = \sqrt{2S_{ij}S_{ij}}$, and $S_{ij} = \frac{1}{2}(\frac{\partial U_i}{\partial x_j} + \frac{\partial U_j}{\partial x_i})$ the components of the mean strain tensor. The term G_b accounts for the suppression of turbulence from density stratification and it is modeled as $G_b = -g_i \mu_t \rho Pr \frac{\partial \rho}{\partial x_i}$, where Pr is the Prandtl number which is taken here to be 0.85. Empirical formulations are commonly employed for the definition of $C_{3\epsilon}$. Here the expression recommended by *Henkes et al.* [1991] and *Heindel et al.* [1994], namely $C_{3\epsilon} = \tanh |\frac{v}{u}|$, is retained, where u and v are the components of velocity normal and tangential to the gravitational vector, respectively.

[11] The term R_ϵ accounts for the effect of the mean strain rate upon the development of ϵ, namely

$$R_\epsilon = \frac{C_\mu \rho \eta^3 (1 - \eta/\eta_0)}{1 + \beta \eta^3 \frac{\epsilon^2}{k}}, \tag{8}$$

where η/η_0 represents the strain rate, being $\eta = S\frac{k}{\epsilon}$ and the constants $\eta_0 = 4.38$ and $\beta = 0.012$.

[12] The density ρ in equations (1) and (2) is defined as of a linear function of the concentration of the solute in the saline. This can be formulated, in FLUENT, by means of a User Defined Function of the form:

$$\rho = (1 - C)\rho_w + C\rho_s \tag{9}$$

here ρ_w and ρ_s represent the density of the ambient fluid in the domain before the saline is released through the inlet and the density of the saline at the channel inflow, respectively. The mass fraction and the concentration of the transported specie are related to each other by $C = \alpha Y_s$, provided that α is prescribed so that $C = 1$ at the channel inflow. The dispersion of the saline is accounted for by means of a transport equation for the mass fraction of the transported specie:

$$\rho_s \frac{\partial Y_s}{\partial t} + \rho_s \nabla Y_s U_i = -\nabla J_s. \tag{10}$$

J_s defines the diffusion of the saline component:

$$J_s = -\left(\rho_s D_s + \frac{\mu_t}{Sc}\right)\nabla Y_s, \tag{11}$$

here $D_s = 5.22\text{e-}09$ m^2 s^{-1} is the coefficient of laminar diffusivity of salt into fresh water and Sc is the Schmidt number taken here equal to unity.

2.2. Near-Wall Treatment

[13] The original work of *Imran et al.* [2004] made use of the standard wall-function method of *Launder and Spalding* [1974] for the near bed flow modeling. In this paper an "enhanced near-wall treatment" based on the models of *Wolfstein* [1969], *Kader* [1981] and *Chen and Patel* [1988] has been employed.

[14] In this case special mesh requirements need to be fulfilled in order for the model to operate adequately. Having defined u_τ and y_p as the friction velocity and the wall-adjacent cell center distance from the wall, the factor $y^+ = \frac{\rho u_\tau y_p}{\mu_t}$ in the wall-adjacent cells has to fall within a prescribed interval. FLUENT recommends that $y^+ \approx 1$ for the "enhanced near-wall" treatment.

[15] This near-wall treatment model aims at resolving the flow features all the way down to the region in the proximity to the wall where a laminar regime occurs due to the viscous effects overwhelming the turbulent ones. This approach treats the flow domain by dividing it into two main regions according to a wall-distance-based Reynolds number, $Re_n = \rho n \sqrt{\frac{k}{\mu_t}}$, where n represents the normal distance from the wall to the center of the first cell. The value $Re_n = 200$ is defined as the border between the viscosity-affected and the fully turbulent regions of the flow. In the viscosity-affected layer, the eddy viscosity and the dissipation of turbulent kinetic energy are defined according to *Wolfstein* [1969] and *Chen and Patel* [1988], respectively. The equations for the velocity and species mass fractions are formulated, in this region of the flow, in such a way that smooth blending of these quantities is achieved across the transition from the laminar to the turbulent layer [*Kader*, 1981].

3. Model Setup

[16] The model described in section 2 is employed for predicting the flow structure at quasi-steady state of a saline density current in a sinuous submerged channel laterally confined by vertical walls. The basal geometry is analogous to the one given by *Ikeda and Nishimura* [1986] and *Kassem and Imran* [2004]. The channel is designed with a sinuosity of 1.13, a minimum centerline radius of 0.684 m and an angular amplitude of 40°. The wavelength of the centerline of the channel is 3.0 m and the channel width is 0.3 m; see Figures 1 and 2a. Two 1.5 m long straight reaches bound the channel at the upstream and downstream end. The channel is confined on both sides by 0.5 m high vertical walls, as opposed to the 1.0 m of *Kassem and Imran* [2004]. The whole domain is subdivided into 300 × 30 × 78 cells (Figure 2b), while the original model of *Kassem and Imran* [2004] was discretized using 70 × 10 × 30. The vertical direction is discretized with a total of 78 cells, 33 of which are located in the region through which the saline travels. The size of the bed-adjacent cells is chosen so that $y^+ < 1$ at all times, according to the near-wall treatment modeling requirements; see section 2.1.

[17] In order to compare directly against existing laboratory and numerical studies the present simulations are run at laboratory scale. Furthermore, boundary conditions are kept as similar as possible with the existing model studies, necessitating a simple rectangular cross section, rather than

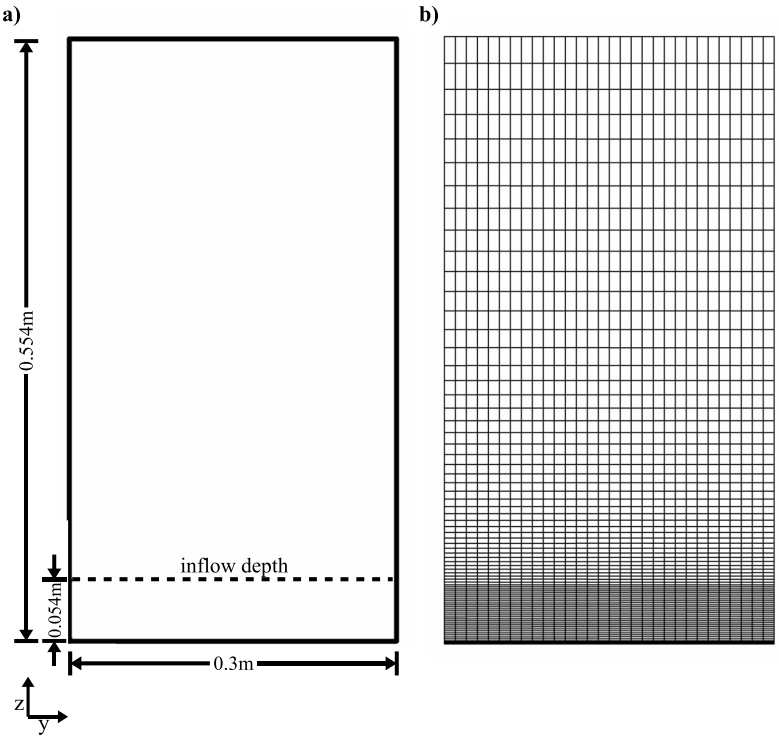

Figure 2. Cross section of the channel. (a) The extent of the area where the saline flow occurs, hence the actual channel, and where the still ambient fluid is stored is depicted. (b) The mesh adopted and the clustering in the actual channel is shown.

the lower angle side slopes typical of submarine channels [*Pirmez and Flood*, 1995; *Babonneau et al.*, 2002]. Given that intrachannel flow in submarine channels is known to interact strongly with overbank flow, with flow exiting and in places reentering the channel [*Keevil et al.*, 2007; *Straub et al.*, 2008; *Islam et al.*, 2008; *Amos et al.*, 2010], and our rationale to elucidate the primary intrachannel flow characteristics herein, then results have only been computed in the domain extending directly upward from the vertical channel sidewalls.

[18] These model simulations represent a generic modeling approach where a degree of dynamic similarity is achieved by maintaining the Froude number for the model at approximately the same value as the prototype [*Eaton and Church*, 2004; *Peakall et al.*, 2007a; *Kane et al.*, 2008]. For flows in submarine channels, scale modeling approaches such as those adopted in some fluvial studies [e.g. *Ashmore*, 1982; *Moreton et al.*, 2002; *Peakall et al.*, 2007b] are not possible, since flow measurements from natural systems are insufficient to provide the prototype or generic data required. Ultimately, CFD modeling at a range of scales is required in order to address the issues of scaling to natural sized flows. That said, this generic modeling approach, while not scaling all variables such as discharge and concentration (currently unknown for submarine channels), has, along with simpler analogue models, proven to be a powerful tool for understanding sedimentary systems [e.g., *Schumm et al.*, 1987; *Peakall et al.*, 1996, 2007b; *Paola et al.*, 2009].

3.1. Initial and Boundary Conditions

[19] The domain is initially filled with still ambient fluid. A saline flow is introduced continuously from an inlet located at the upstream end of the channel. The deeper part of the domain, which extends from 0 to 0.054 m along the vertical direction, is regarded as the actual channel, where fixed, no slip walls constrain the lateral displacement of the saline. Above the levee height, free-slip boundaries are prescribed on the lateral side of the domain and at the top boundary parallel to the channel bed. Boundary conditions are prescribed as follows:

[20] 1. A flow inlet condition at the upstream end of the channel, $x = 0.0$ m, $0.0 < y < 0.3$ m, $0.0 < z < 0.054$ m, from which a 1032 kg m^{-3} dense saline is introduced at a speed of 0.16 m s^{-1}. The turbulence intensity $I = 0.16 Re_{d_h}^{-\frac{1}{8}}$, with Re_{d_h} being the Reynolds number estimated on the hydraulic diameter d_h for rectangular pipes is prescribed along with the turbulence length scale l. The turbulence length scale can be estimated from $l = 0.07 d_h$, $l = C_\mu \frac{k^{\frac{3}{2}}}{\epsilon}$ or, for the case of wall bounded inlets, $l = \frac{1}{2} 0.37 Re^{-\frac{1}{5}}$ [*Schlichting*, 1968]. The values imposed for I and l are 4.8% and 0.004 m, respectively.

[21] 2. An open pressure outlet at the downstream end of the channel, $x = 6.8$ m, $0.0 < y < 0.3$ m and $0.0 < z < 0.5$ m, defined by $\frac{\partial U}{\partial x}, \frac{\partial V}{\partial x}, \frac{\partial W}{\partial x} = 0.0$ m s^{-1}, $\frac{\partial k_t}{\partial x} = 0.0$ m^2 s^{-2}, $\frac{\partial \epsilon_t}{\partial x} = 0.0$ m^2 s^{-3}, $\frac{\partial Y_s}{\partial x} = 0.0$.

[22] 3. Fixed-wall, no slip boundaries at the channel bed and the lateral sides of the channel bed.

[23] 4. Free-slip boundaries at the vertical boundaries above the lateral sides of the channel bed and at the top boundary of the domain.

[24] Initial conditions are defined by the domain initially filled with fresh water of density 998.2 kg m^{-3} and salt mass fraction $Y_s = 0.0$; turbulent parameters are set to $k = 0.001$ m^2 s^{-2}, $\epsilon = 0.001$ m^2 s^{-3}, in accordance with *Corney* [2005].

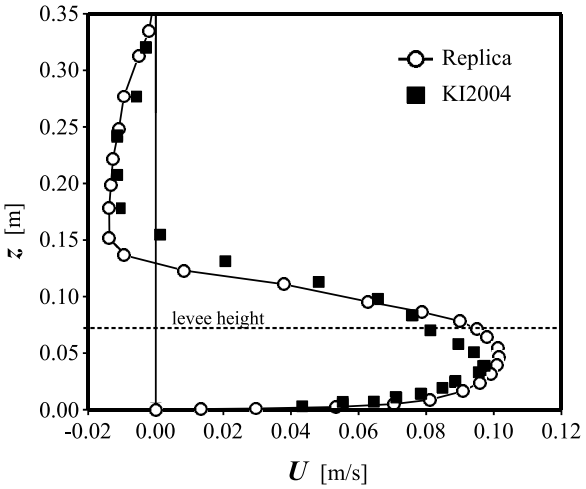

Figure 3. Comparison of the downstream component of velocity at the channel axis of the first bend from *Kassem and Imran* [2004] and the present simulation with the enhanced wall treatment approach. Axial slope of 0.08°.

A time step equal to 0.1 s proved to be suitable for solution convergence and accuracy, as found by *Imran et al.* [2004] and *Kassem and Imran* [2004]. The simulations are performed in transient mode in order to facilitate solution convergence. The dense flow is released from the inlet and allowed to reach the downstream end of the channel. At this point the continuity, momentum and transport equations and the drag coefficient at the channel bed are monitored until a converged solution is reached. The results achieved in this manner are found to be an accurate representation of the flow at steady state.

3.2. Experiments Description

[25] The aim of the analysis is to attempt to explain the mechanics which regulate the occurrence of river-like and river-reversed secondary circulations. It has been observed that contradictory outcomes are achieved by different authors even when fairly similar geometrical features and flow conditions are being investigated. Some evidence has been provided that the onset of a river-reversed secondary circulation may not be dependent on factors such as scale, axial slope, and geometrical features of the planform and channel bed cross section [*Keevil et al.*, 2007]. Nevertheless, the hypothesis is made here that a more exhaustive investigation of the effect of the axial slope tilting is required in order to fully uncover the potential of this term in regulating the intra-channel cross-sectional circulation. The geometry of *Kassem and Imran* [2004] is chosen as the test case. A set of four numerical experiments are executed, each performed at an increasing slope of the channel axis, equivalent to 0.08°, 0.43°, 1.5° and 2.5°, respectively. The 0.08° and 0.43° tests are intended to replicate the *Kassem and Imran* [2004], the *Islam and Imran* [2008] and the *Imran et al.* [2007] numerical and physical experiments, which all concordantly underscored the occurrence of the river-like secondary circulation. The latter two expand the analysis over the gap which extends between the configurations adopted by *Islam and Imran* [2008] and *Keevil et al.* [2006]. This set of experiments aims at covering an ensemble of suitable values of axial slopes at which physical simulations are performed in the laboratory [*Middleton*, 1966].

4. Validation of the Previous Work

[26] A first simulation analogous to the case investigated by *Kassem and Imran* [2004] for the enclosed sinuous channel (0.08° tilt of the planform geometry) is performed and quantitative comparison with the results of *Kassem and Imran* [2004] is provided in Figures 3, 4 and 5. The downstream component of velocity at the channel axis of bend 1 at steady state is shown in Figure 3, confirming the occurrence of solutions which are very close to those described by *Kassem and Imran* [2004]. Differences in the solution data set can be either attributed to the employment of a higher degree of mesh resolution or the establishment of a boundary layer resolving approach. In the latter case, the turbulent quantities were not reported by *Kassem and Imran* [2004]. Also strong similarities, both in qualitative and quantitative terms, are found in the cross-stream velocity at the channel axis of bend 1, as displayed in Figure 4. The main difference is that the refined model has a core of outward moving momentum above the levee height. However, the overall river-like behavior is found to occur as postulated by *Kassem and Imran* [2004]; see Figure 5.

[27] Given the consistency with the results of *Kassem and Imran* [2004] at an axial slope of 0.08°, the numerical model is then employed for predictions at 0.43°, in line with the experiment of *Islam and Imran* [2008]. Despite the differences in planform geometry and scale, significant similarities may be underscored with the configuration accounted for by *Islam and Imran* [2008]. All the quantities predicted by the

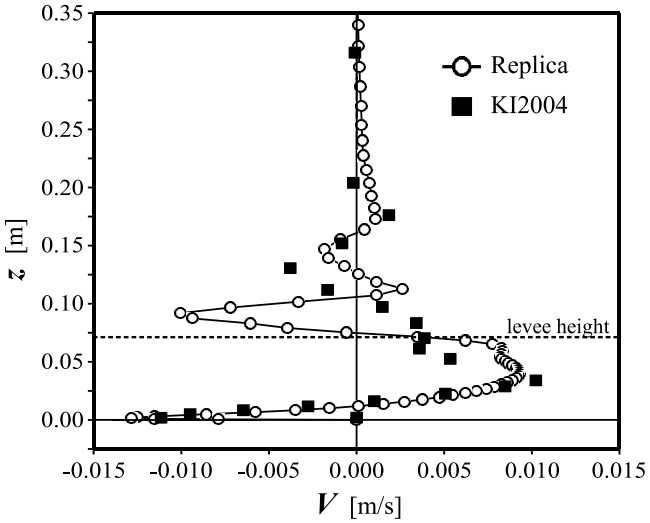

Figure 4. Comparison of the cross-stream component of velocity at the channel axis at the first bend from *Kassem and Imran* [2004] and the present simulation with the enhanced wall treatment approach at an axial slope of 0.08°. Positive velocity values are oriented toward the outer bank, while negative values are toward the inner bank.

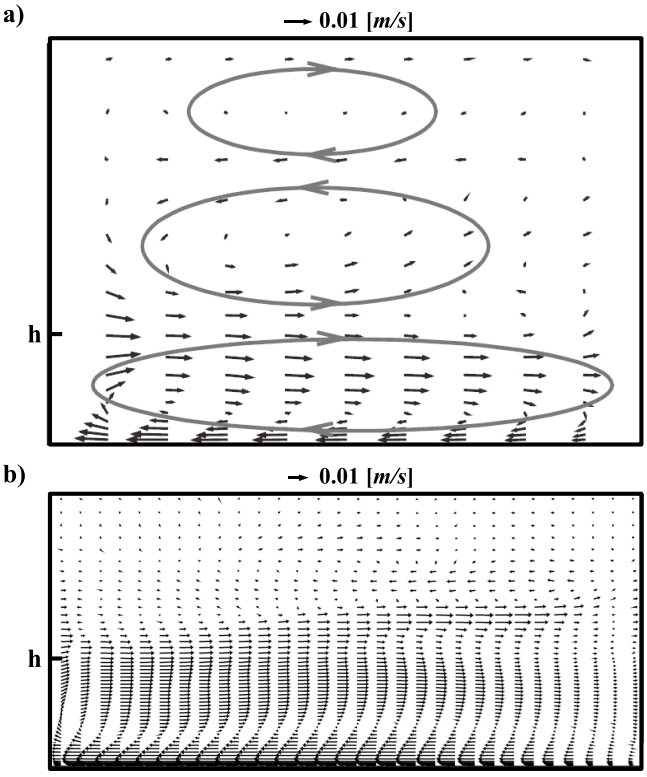

Figure 5. Comparison of the cross-stream vector field at bend 1 between the results of (a) *Kassem and Imran* [2004] and (b) the present numerical model.

numerical model are nondimensionalized and compared to the measurements from the physical experiment of *Islam and Imran* [2008] (Figures 6 and 7). It is observed that there is an excellent fit for both the downstream component of velocity and the turbulent kinetic energy at the channel axis of bend 1.

[28] The degree of consistency perceived by the present model with the preexisting numerical and experimental investigations both confirms the numerical simulations of *Kassem and Imran* [2004] and reinforces the results of *Islam and Imran* [2008]. Also, it allows the present model to be confidently adopted for assessing how the flow patterns respond to increased values of the axial slope.

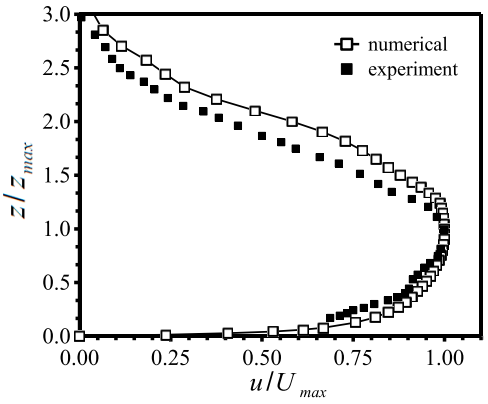

Figure 6. Comparison of the downstream component of the velocity at the channel axis at the first bend from *Islam and Imran* [2008] and the present simulation with the enhanced wall treatment approach. Axial slope of 0.43°.

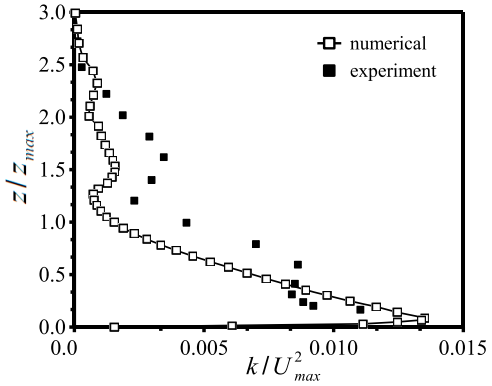

Figure 7. Comparison of the turbulent kinetic energy at the channel axis of the first bend from *Islam and Imran* [2008] and the present simulation with the enhanced wall treatment approach. Axial slope of 0.43°.

5. Flow Response at Axial Slope Variation

[29] Repetition of the same numerical experiment at increasing values of the axial slope is performed for 1.5° and 2.5° and compared with the 0.43° case. In all cases, the saline attains equilibrium before entering the region of curvature of the first bend (Figure 8). When the attention is drawn on the apex of the first bend, outstanding changes are progressively observed as the incline is varied. Results are extracted at four vertical profiles located at increasing distance from the inner bank in the cross section of bend 1. Profiles 1, 2, 3 and 4 of Figures 9, 10, 11 and 12 correspond to locations 0.06, 0.12, 0.18 and 0.24 m, respectively, from the inner bank along the cross-stream direction. This representation clearly depicts what occurs on the two sides of the midchannel axis, where the most relevant flow modifications occur.

5.1. Density

[30] The density manifests a clear trend in that the core of the saline becomes progressively less homogeneous in the bend cross section as the planform is inclined (Figure 9). Given a specific density, the variation of the height above the channel bed from profiles 1 to 4 describes well the tilting of the saline core in the cross-sectional direction. It is observed, for instance, that at the 0.43° inclination (Figure 9a) the vertical height of the 1018 kg m^{-3} isosurface equivalent to about 60% of the initial concentration of the saline at the inlet varies from about 0.054 m (the levee height) at profile 1 (near to the inner bank) to about 0.9 m at profile 4 (near to the outer bank). At 1.5° (Figure 9b), the tilting of the same density isosurface has dramatically increased, mainly due to the inner bank portion of the saline being squeezed against the channel bed. At an inclination of 2.5° such trends are further enhanced. The shape of profile 4 also suggests that a folding of the isosurface has occurred due to the reinforced centrifugal acceleration.

[31] The variation of the saline is found to be extremely susceptible to the steepening of the axial slope when a tilt of 2.5° is achieved (Figure 9c). Variations in the spreading of the saline is apparent both in the vertical and in the cross-

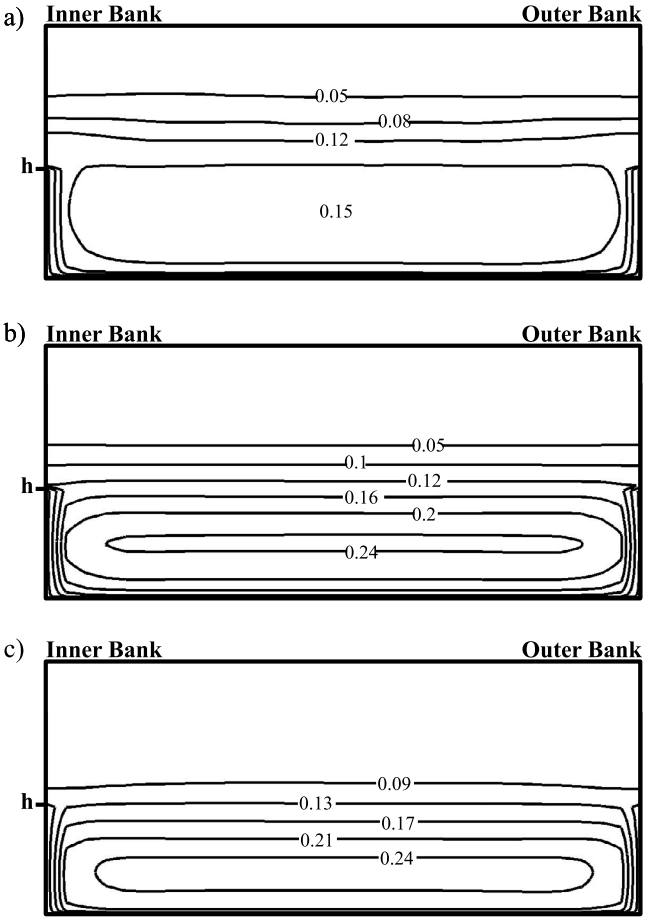

Figure 8. Isocontours of the downstream velocity in m s^{-1} at a cross section 0.4 m upstream of the first bend for the cases (a) 0.43°, (b) 1.5°, and (c) 2.5°.

sectional directions. The core of the saline, initially occupying the entire vertical extent of the channel depth, is eventually displaced below the levee height (Figure 9a). The major part of the most concentrated portion of the density current has also been visibly shifted toward the outer bank. Such a displacement plays a remarkable role both in determining the three-dimensional structure of the momentum field and the local Froude number of the flow, as discussed in sections 6.2 and 7.

5.2. Downstream Velocity

[32] At increasing axial slopes, the horizontal component of the velocity displays a behavior consistent with that of the density field. The overall trend entails that the height of the maximum downstream velocity, U_{max} progressively declines from half the channel height to the proximity of the channel bed as slope increases. In analogy with the overall tilting of the flow as observed for the density, the velocity maximums are lowest toward the inner bank, increasing across the channel toward the outer bank. The regions of the saline nearer to the inner bank are those more exposed to the vertical displacement of the velocity maximum. Profile 1 is where the core of the downstream velocity is subject to the largest vertical displacement, where the U_{max} shifts from about 0.025 m to less than 0.01 m above the channel bed when the axial gradient is increased from 0.43 to 2.5° (Figures 10b and

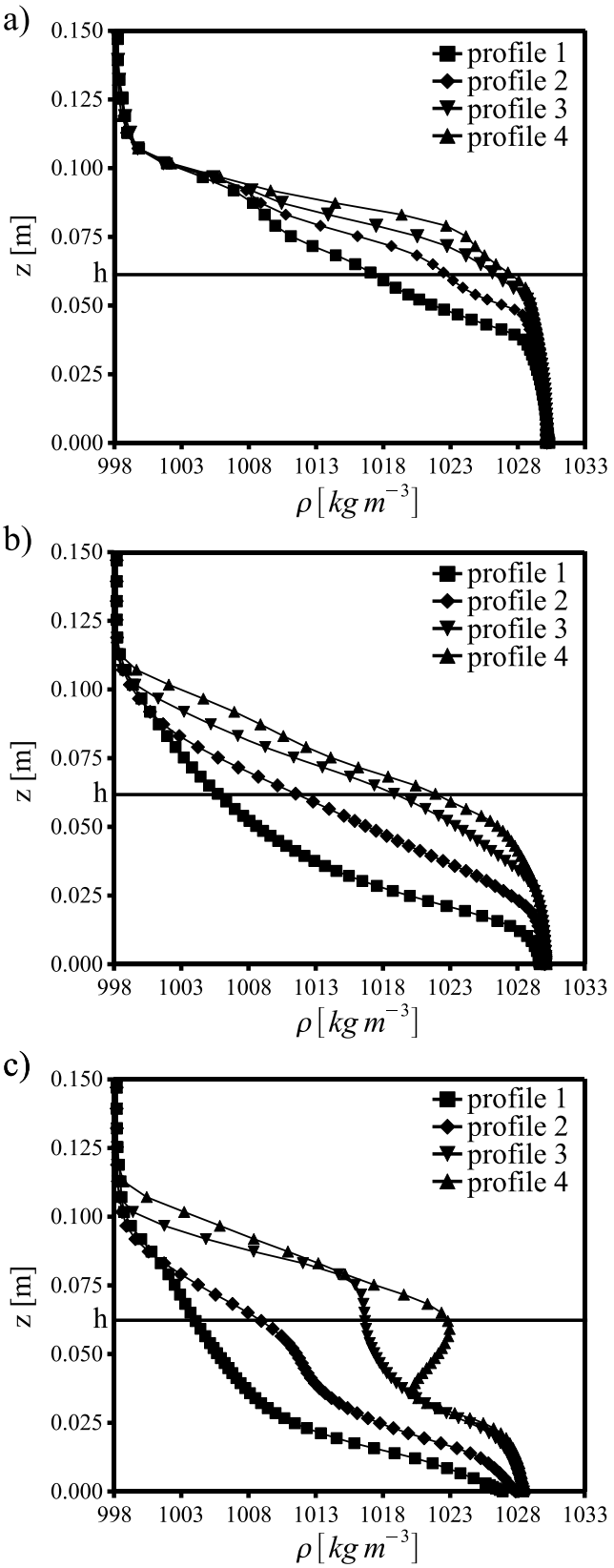

Figure 9. Vertical profiles of the density at the first bend of the channel for an axial slope of (a) 0.43°, (b) 1.5°, and (c) 2.5°. The profiles 1, 2, 3, and 4 are located at 0.06, 0.12, 0.18, and 0.24 m, respectively, from the inner bank along the channel width cross section.

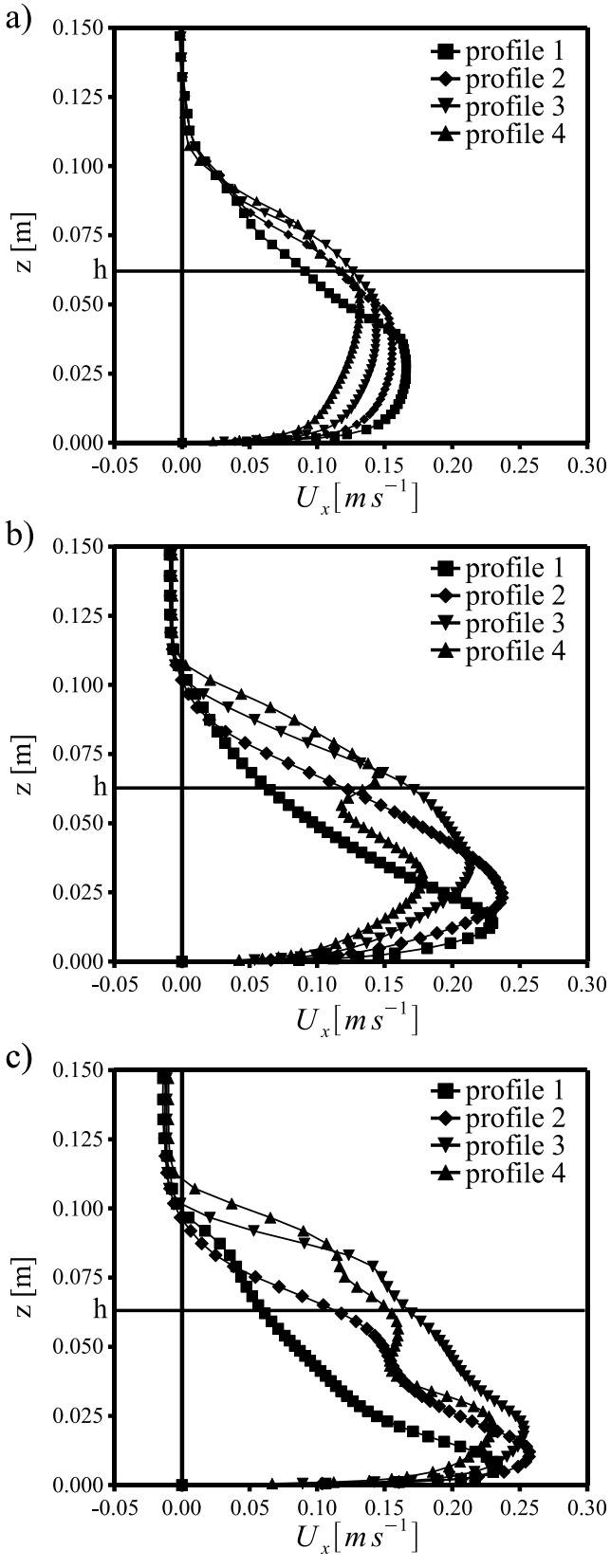

Figure 10. Vertical profiles of the downstream velocity at the first bend of the channel for an axial slope of (a) 0.43°, (b) 1.5°, and (c) 2.5°. The profiles 1, 2, 3, and 4 are located at 0.06, 0.12, 0.18, and 0.24 m, respectively, from the inner bank along the channel width cross section.

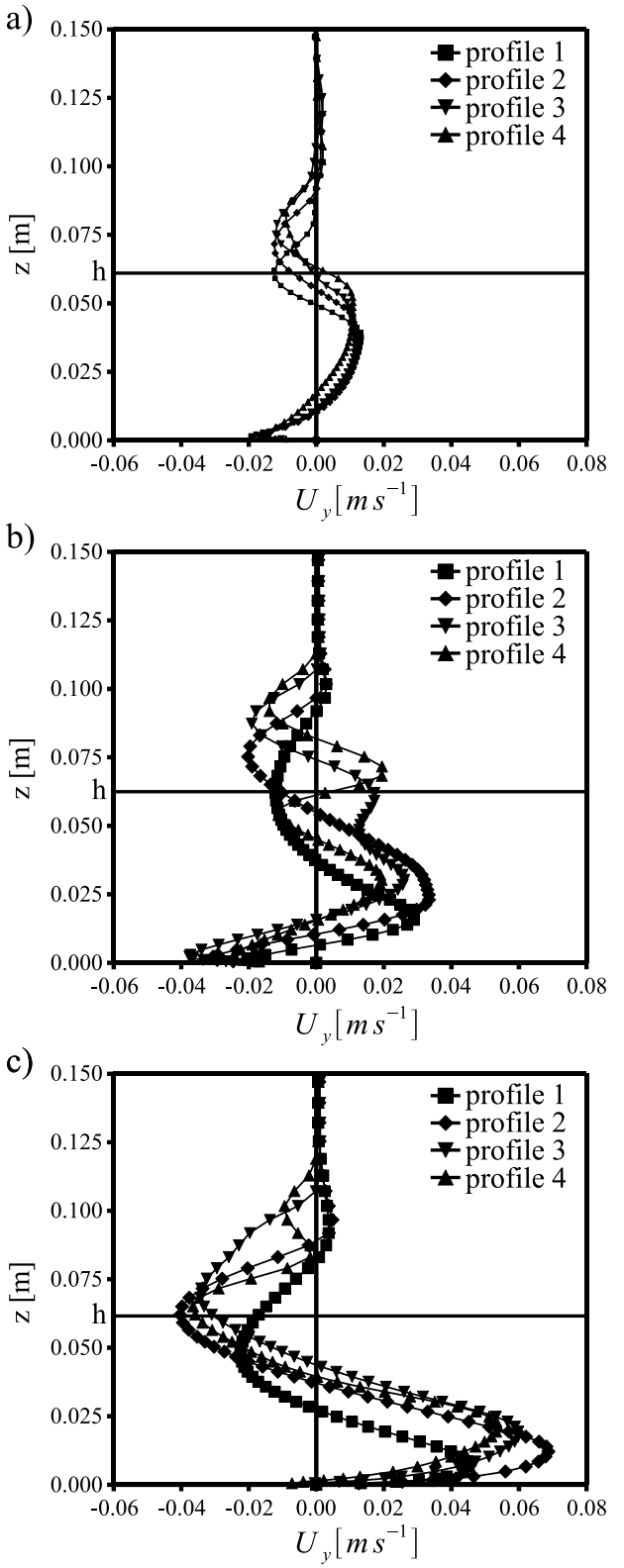

Figure 11. Vertical profiles of the cross-stream velocity at the first bend of the channel for an axial slope of (a) 0.43°, (b) 1.5°, and (c) 2.5°. The profiles 1, 2, 3, and 4 are located at 0.06, 0.12, 0.18, and 0.24 m, respectively, from the inner bank along the channel width cross section. Positive velocity values are oriented toward the outer bank, while negative values are toward the inner bank.

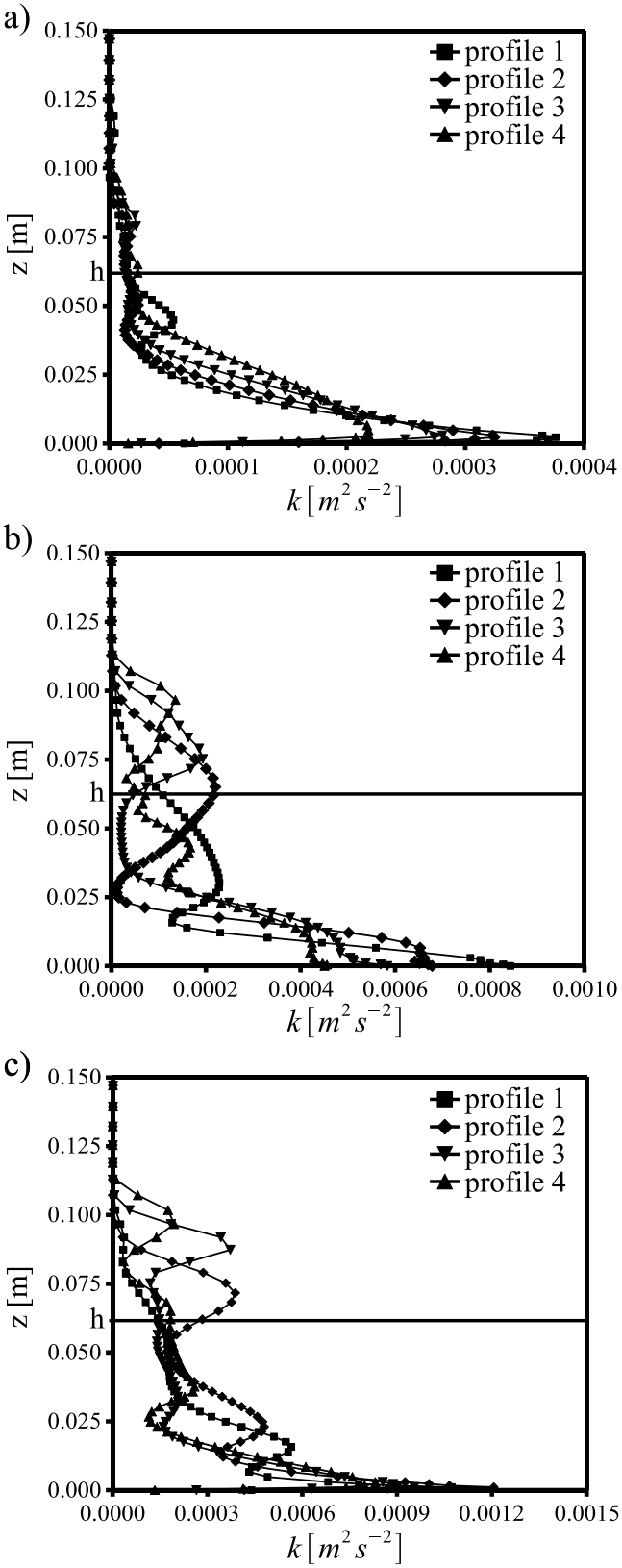

Figure 12. Vertical profiles of the turbulent kinetic energy at the first bend of the channel for an axial slope of (a) 0.43°, (b) 1.5°, and (c) 2.5°. The profiles 1, 2, 3, and 4 are located at 0.06, 0.12, 0.18, and 0.24 m, respectively, from the inner bank along the channel width cross section.

10c). Interestingly, different locations along the cross section manifest different responses to the tilting of the axial slope. While the region nearer to the inner bank readily responds to the 0.43° to 1.5° tilting of the planform incline (Figures 10a and 10b), significant fluctuations in the position of U_{max} for profiles 3 and 4 is underscored when the axial slope is varied from 1.5° to 2.5° (Figures 10b and 10c).

[33] In quantitative terms, profiles 2 and 3 are those where the fastest portion of the density current is observed. The tilting of the planform from 0.43° to 1.5° is responsible for the larger acceleration of the fluid, with a recorded velocity variation of about 65% in the case of the profile located at 0.12 m from the inner bank (profile 2). The profile closer to the inner bank, profile 1, responds to the 0.43° to 1.5° gradient variation with a pronounced change in velocity magnitude, while only a marginal increase in velocity is highlighted during the 1.5° to 2.5° tilting. Profile 4 appears to be the least susceptible, in quantitative terms, to the axial slope steepening. The U_{max} registered near the outer bank varies from 0.13 to 0.18 m s^{-1} between 0.43° and 1.5° (Figures 10a and 10b) and from 0.18 to 0.23 m s^{-1} between 1.5° and 2.5° (Figures 10b and 10c), suggesting a more homogeneous trend in the acceleration.

[34] These observations confirm that different locations of the channel cross section are more sensitive to specific change of the axial slope. In particular, the inner bank portion responds to limited variations, while the outer bank regions require more pronounced tilting in order to manifest noticeable changes. All profiles manifest a remarkable shift in the U_{max} position toward the channel bed and an increase in the U_{max} magnitude.

[35] Comparison of these submarine results can be made with estuarine flows. Estuarine flows have been observed to, in certain cases, exhibit velocity profiles that are nonlogarithmic, with velocity maximums well below the surface and sharp gradients either side of these maximums [*Geyer*, 1993; *Lacy and Monismith*, 2001]. Such profiles in estuarine systems can be associated with either river-reversed [*Lacy and Monismith*, 2001] or river-like [*Geyer*, 1993] secondary flows dependent on the exact form of the velocity profile in combination with other parameters including the density distribution and bend curvature. In estuarine flows, the mode of secondary circulation has been shown to result from a prevailing curvature-regulated flow where centrifugal forcing dominated. In sections 5.3 and 5.4, the correlation which exists between the shape of the vertical profile of downstream velocity and the cross sectional circulation is examined.

5.3. Cross-Stream Velocity

[36] In Figure 11a the cross-stream patterns of velocity for the 0.43° incline are found to be in excellent agreement with the features underscored by *Kassem and Imran* [2004] and *Islam and Imran* [2008]. The main component of the cross-stream flow travels from the inner bank toward the outer bank. The intensity of this outward moving stream, located at half the depth of the channel, is fairly homogeneous across the entire cross section, with a recorded positive V_{max} of 0.013 m s^{-1} for the case of profile 1 and 0.01 m s^{-1} for profile 4. A basal flow directed from the outer to the inner bank of the channel is also observed. This inward directed flow is physically confined to the region in close proximity

with the channel bed and displays higher velocities than the middepth component of the flow. The predicted inward pointing V_{max} for profile 1 at the channel bed is as large as 0.019 m s^{-1}. At the levee height, a reversed, weaker flow compared to the main cross-stream component is observed. A further inward traveling portion of the flow is thus located beyond the levee depth. The whole structure of the velocity field firmly suggests the occurrence of a main, circular, cross-stream flow pattern with a distinct clockwise orientation for an observer located downstream of the channel bend.

[37] As the incline of the plane increases to 1.5°, the overall flow pattern remains qualitatively stable. The main changes affect the location of the local V_{max}. The entire cross-stream flow appears to shift vertically downward toward the channel bed. The profiles more closely located to the inner bank of the channel are the ones more severely affected in this sense.

[38] Consequently, the primary outcome of the steepening of the planform is a significant increase in the cross-stream velocity magnitude, both for the outer bank (profile 1 and 2) and the inner bank (profile 3 and 4) oriented components of the flow. Secondly, all profiles bring evidence of a large drop in the depth of the V_{max}. The outward pointing V_{max} are thus displaced from a depth near to the levee height to a location below this and well within the actual channel. Furthermore, in the case of profile 1 and 4, negative and important local V_{max} are observed not only well below the levees, but also at the levee height. This implies that the flow pattern previously highlighted for the case with a 0.43° incline has been modified in two ways. First, the main circular clockwise rotating orbit has been squeezed toward the bottom of the channel. Second, a subordinate, yet nonnegligible, anticlockwise revolving stream has developed in the higher portion of the channel below the levee height.

[39] At the axial slope of 2.5° the solution manifests outstanding changes which result in a total overturn of the secondary circulation (Figure 11c). The most striking end result is the reversal of the basal component of the flow. From being oriented toward the inner bend at 1.5° inclination, the entire cross section of the channel bend presents a stream located at the channel bed which flows from the inner to the outer bank. This is in agreement with the observations of *Keevil et al.* [2006, 2007]. In parallel with the positive, basal V_{max}, a negative maximum, inward pointing V is generated at the same height of the levees of the channel. These observations are fairly homogeneous throughout the whole cross section of the channel, with very strong similarities over the different profiles both in terms of the depth of the V negative maximum and their magnitude. The interpretation of this newly established flow pattern is apparent. A dominant, strong, basal stream oriented from the inner to the outer bank is observed in conjunction with a return flow of a comparable intensity located at the levee height. The overall circulation is readily interpreted as a single, clearly visible cell rotating anticlockwise for an observer looking into the cross section from downstream of the channel bend. This final result is in excellent agreement with the observations presented by *Keevil et al.* [2006, 2007] and the analytical model of *Corney et al.* [2006, 2008].

5.4. Turbulent Kinetic Energy

[40] In Figure 12 the four vertical profiles of the turbulent kinetic energy are presented at increasing values of the planform tilt. The tilting of the axial slope causes three clearly distinct stages. At an axial slope of 0.43°, two regions with high and low levels of turbulence are located at half the channel depth and at the channel bed, respectively. At an inclination of 1.5° the bed-adjacent turbulence remains consistent with the 0.43° case, but additional locations of low and high turbulence production are formed at variable depths along the cross section of the bend. This appears as a transitional phase marked by the onset of a complex structure of recirculating zones. Further steepening of the axial slope finally causes the turbulence structure to shift again to a pattern which is qualitatively similar to the initial case with a 0.43° inclination, where a high turbulence region confined to the channel bed is overlain by a low turbulence region in the lower half of the channel depth. This suggests that the cross-stream flow with a 2.5° tilt is again dominated by a main shearing region confined to the proximity of the channel bed and a thick homogeneous flow of fluid traveling at half the channel depth.

6. Two-Dimensional Flow Analysis

[41] It has been shown in section 5 that tilting of the axial slope from 0.43° to 2.5° caused the flow to shift from a river-like to a river-reversed secondary circulation. The transition from one orientation to the other appears to undergo a stage where complex flow patterns occur. In order to comprehend the processes involved with the overturning of the secondary circulation, a clear visualization of the transitional process is required.

6.1. Cross-Sectional Field of Downstream Velocity

[42] The role of the downstream component of the velocity, and in particular its two-dimensional structure in the channel cross section, has been proved to be relevant in determining the triggering of the transition from one mode of secondary circulation to the other [*Corney et al.*, 2008; *Nidzieko et al.*, 2009]. Therefore, the evolution of the downstream velocity field as a result of the progressive sloping of the planform is examined in Figure 13.

[43] The intra channel flow, below the levee height, presents a core where more intense downstream velocities are observed as the planform is tilted. The core of velocity changes in magnitude, spatial extent and position in the channel cross section. At the lowest gradient, Figure 13a, the region of maximum downstream velocity is located in the half of the channel closest to the inner bank, at a considerable distance from the bed. Due to the centrifugal acceleration, the outward facing border of the core is stretched along the cross section of the bend. The isocontours of velocity present a regular pattern. The higher velocities, from 0.17 to 0.095 m s^{-1}, are homogeneously scattered around the innermost core and manifest the same outward stretching of the innermost isocontour along the inner to the outer bank direction. The isocontours associated with the lower velocities are regularly spread along the vertical direction and thus show evidence that only a very mild cross-stream tilting of the velocity gradient is produced.

[44] At a 1.5° axial slope, Figure 13b, the cross-sectional downstream component of velocity responds in the following ways. The velocity magnitude in the core grows from 0.17 to 0.245 m s^{-1} and shifts closer to the channel bed. The core

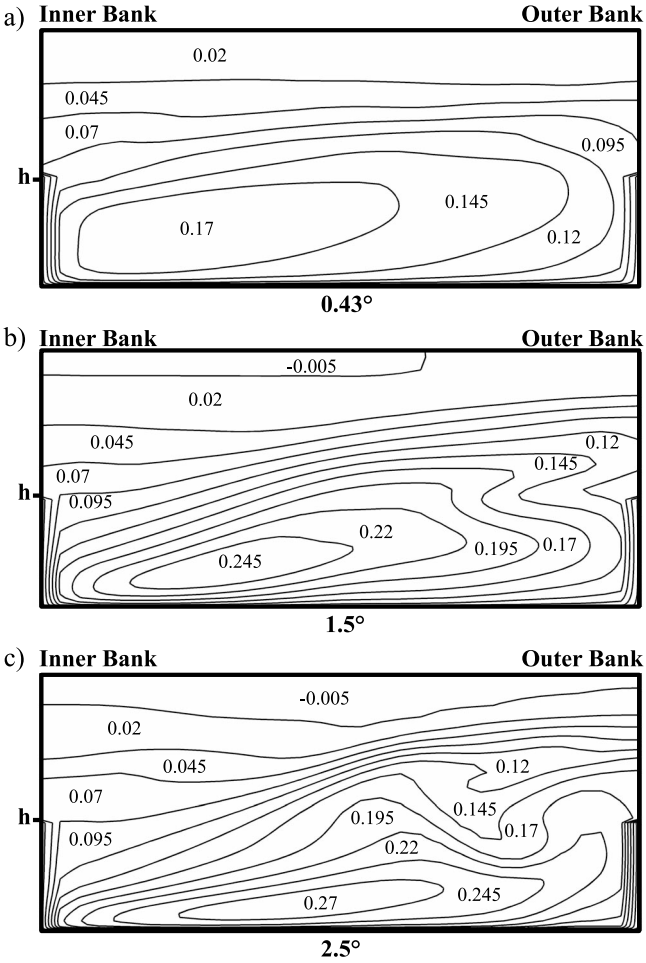

Figure 13. Isocontours of the downstream velocity at the cross section of the first channel bend for the cases (a) 0.43°, (b) 1.5°, and (c) 2.5°.

becomes squeezed and stretched by centrifugal force to the point where an elongated shape in the cross-stream direction is assumed and the isocontours of velocity present a visible cross-stream tilting along the outward direction.

[45] As a result of further steepening to 2.5°, Figure 13c, the features identified at an inclination of 1.5° become heightened. In particular, the velocity core flattens against the channel bed, stretches along the inner to outer bank direction and shifts to the middle of the channel width [see also *Keevil et al.*, 2006]. The investigation of the downstream component of velocity at the channel cross section allows to better interpret the development of the cross-stream circulation at the channel apexes.

6.2. Cross-Stream Vector Field

[46] In Figure 14 the vector fields for the flows associated with the 0.43°, 1.5° and 2.5° axial slopes are displayed. The case with the lowest inclination, Figure 14a, is comparable to the single bend submerged channel of *Imran et al.* [2007] and *Islam and Imran* [2008]. Here it is confirmed that the solution deployed by the present numerical model matches the results presented in Figure 2 of the paper by *Imran et al.* [2008] and by *Imran et al.* [2007], though the inclusion of a more detailed wall function seems to lead to a reduction in basal flow velocities relative to *Imran et al.* [2008]. The principal component of the flow travels from the inner to the outer bank and concerns the wide portion of the cross section confined between the levee height and the bed-adjacent region (Figure 14a). At the outer bank levee, the main stream undergoes a separation which splits the flow in two. The downward and upward branches of the flow give rise to a velocity structure defined by a lower clockwise cell with a basal inward component and an anticlockwise cell around the levee height, respectively.

[47] From Figure 14b it is now clear that increasing the tilt of the experimental rig to 1.5° pushes the main outward traveling flow deeper and causes new recirculating zones to develop, thus initiating the process of transition of the secondary circulation from river-like to river-reversed. The main outward traveling flow impacts with the outer bank levee at a depth below the levee height (Figure 14b). From the flow separation near the outer bank, two minor flow cells are produced at the channel bed and at the levee depth (Figure 14b), respectively. The bottom cell occupies the right hand side of the bed-adjacent region. This cell appears to be extremely important in regulating the bed flow from the outer to the inner bank. In particular the basal flow looks stronger in the region close to the bed underneath this cell. On the

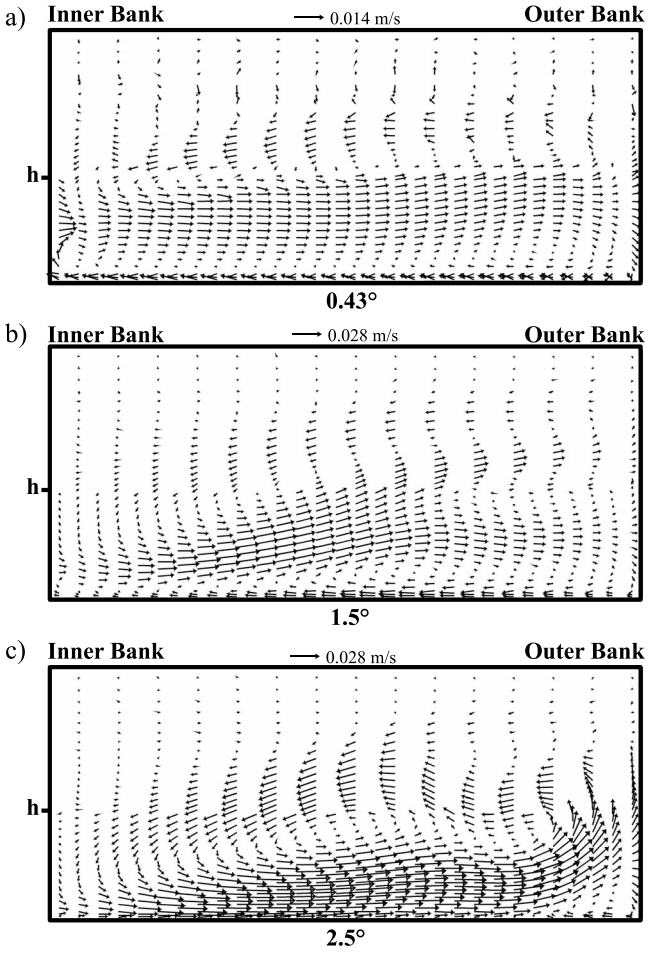

Figure 14. Vector plot of the cross-stream velocity at the first bend cross section of the channel for cases (a) 0.43°, (b) 1.5°, and (c) 2.5°. The label h is the levee height.

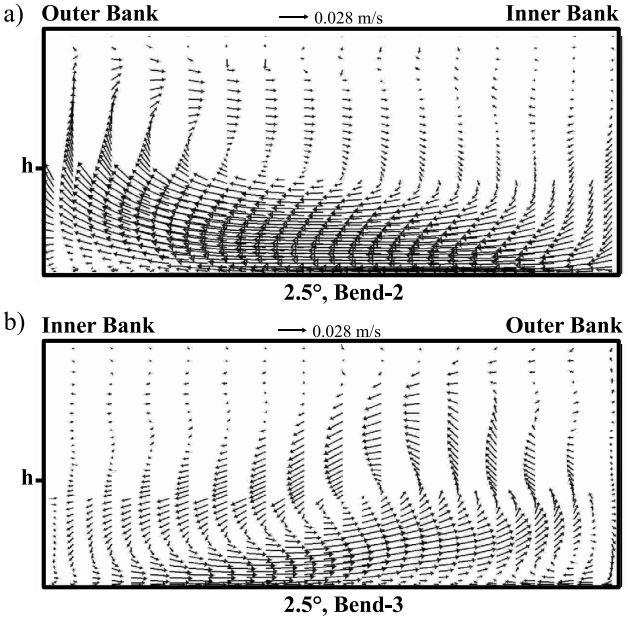

Figure 15. Vector plot of the cross-stream velocity at channel apex cross sections for (a) the second bend and (b) the third bend for a 2.5° inclination of the axial slope. The label h is the levee height.

other hand, the flow in proximity of the channel bed appears weaker at the two ends of this flow cell and it is almost annihilated close to the inner bank, as confirmed by the bottom V values of profile 1 in Figure 11b. A remarkable element is the development of a further anticlockwise revolving cell at the levee height of the inner side of the channel cross section. The core of maximum downstream velocity discussed in section 6.1 (Figure 13b) lies precisely underneath this anticlockwise rotating vortex (Figure 14b). This recirculating zone becomes dominating as the slope is further increased to 2.5°, when the anticlockwise rotating cell grows bigger and shifts closer to the midchannel axis and thus controlling the whole flow system (Figure 14c). The position of the core of downstream velocity (Figure 13c) appears once more to be associated with the new position of this anticlockwise rotating vortex. The main body of the flow traveling from the inner to the outer bank is now confined to the bottom of the channel by the central anticlockwise flow cell. This strong, outward moving flow pushes the clockwise rotating cell previously observed at the channel bed (Figure 14b) to the bottom corner of the outer bank levee (Figure 14c). This bottom flow cell, which appears to be the remnant of the inward flowing basal stream typical of the river-like circulation is now almost totally annihilated.

[48] With the basal flow cell shrunk to a marginal recirculating zone, and the overall flow system controlled by a

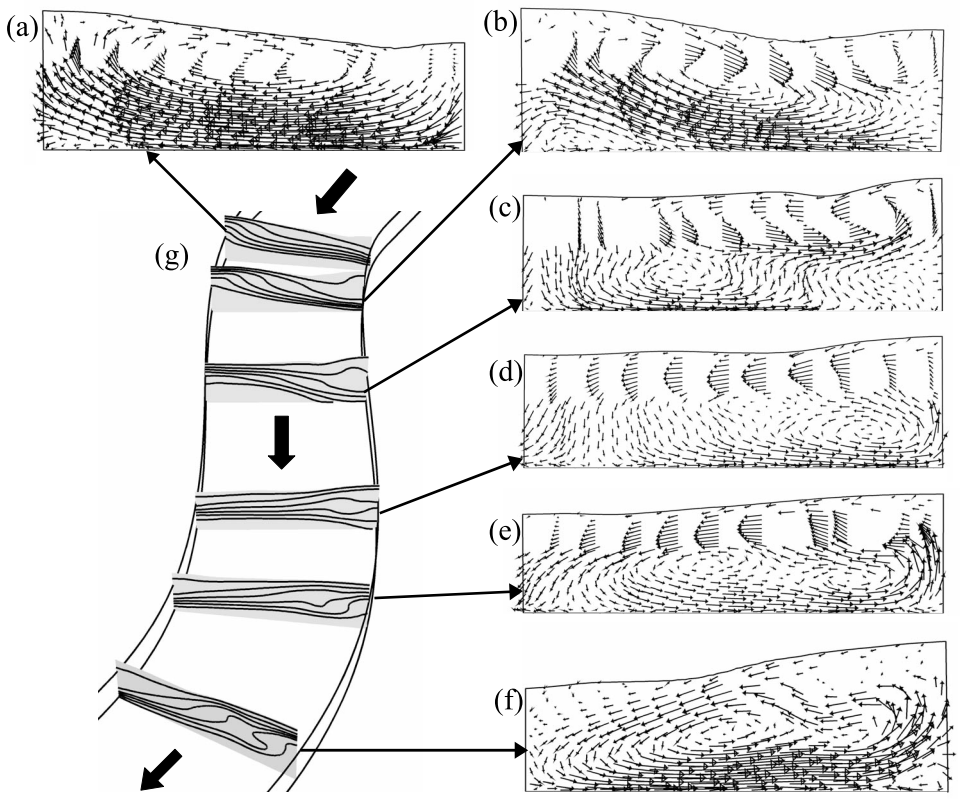

Figure 16. Vector plot of the cross-stream velocity within the 2.5% isopycnal at several cross sections located between the straight reach and the first bend apex of the channel when tilted 2.5°. Figure 16a refers to the plane at the end of the straight reach of the channel, 1.6 m downstream of the inflow; see Figure 1. Figure 16f refers to the plane at the apex of the first bend; see also Figure 14a. Figure 16g shows the 2.5, 5, 10, 20, 40, 60, and 80% is contours of concentration at the six planes; the black thick arrows represent the major downstream component of the flow.

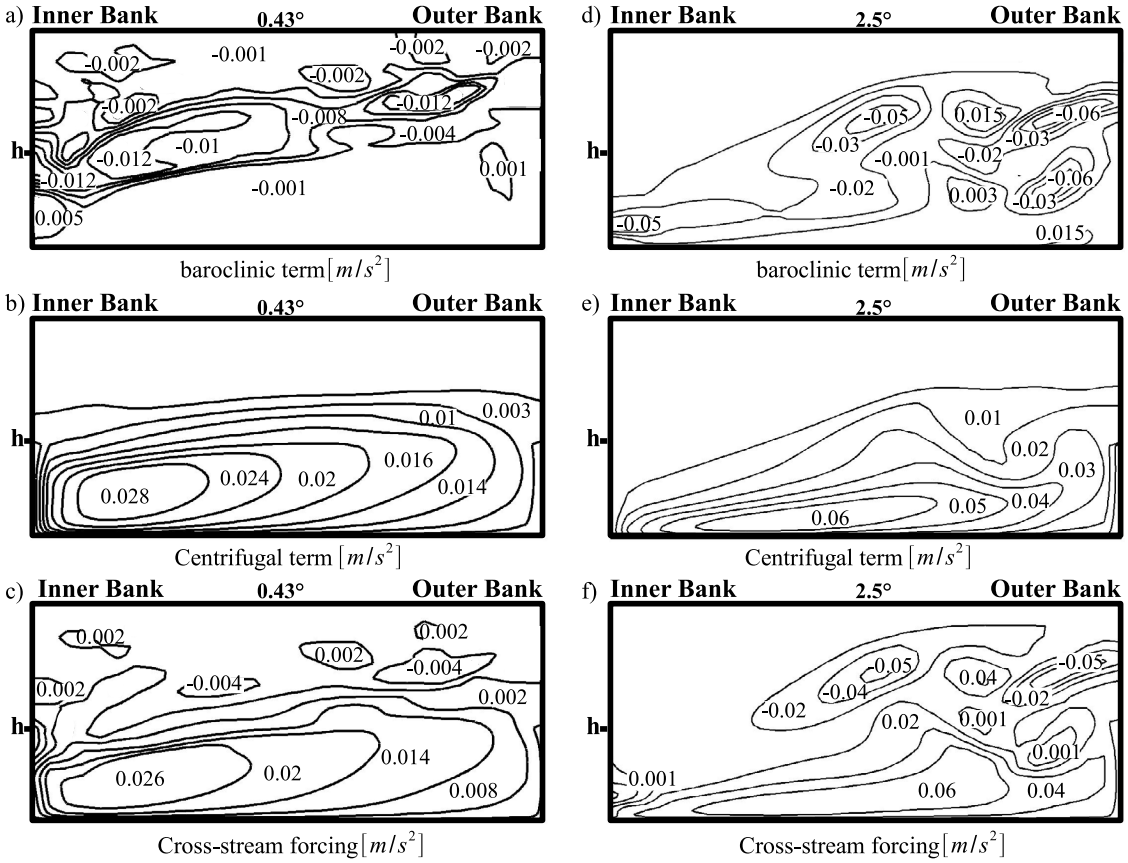

Figure 17. (a and d) Baroclinic and (b and e) centrifugal terms and (c and f) their difference at the apex of the first bend for the 0.43° and the 2.5° axial slopes. Negative values are directed toward the inner bank.

single, dominant, anticlockwise circulation, the transition to a river-reversed secondary cross-stream pattern may be considered accomplished. Attainment of the river-reversed mode of circulation throughout the channel is confirmed by the cross-stream flow pattern at bend 2 and bend 3; see Figure 15.

6.3. The Baroclinic-Centrifugal Equilibrium

[49] The transition from one mode of circulation to another has been repeatedly observed in estuarine systems [*Chant and Wilson*, 1997; *Lacy and Monismith*, 2001; *Cheng et al.*, 2009]. The measurements from tidal processes aid in evaluating the mechanism which controls the overturn of the secondary circulation. In section 5.2 the comparison between vertical profiles of downstream velocity in submarine channels and estuarine environments was drawn, emphasizing how highly nonlogarithmic profiles were recorded by *Lacy and Monismith* [2001]. Most importantly, the highly nonlogarithmic velocity maxima located deep in the water column, the mild curvature and the occurrence of a cross channel density gradient permitted the establishment of a baroclinic-centrifugal balance. Interestingly, the oscillations of this unstable equilibrium supported both a river-like and a river-reversed transverse circulation, associated with prevailing baroclinic pressure gradients and centrifugal force, respectively [*Lacy and Monismith*, 2001]. The alternation of phases during which baroclinic pressure gradient and centrifugal forces are predominant one over the other depends either on the position of the flow along the curvature, or on the intensity of the stratification [*Lacy and Monismith*, 2001; *Nidzieko et al.*, 2009].

[50] In analogy with flood and ebb tide in estuaries, a saline density current in a curved channel experiences a smooth transition along the baroclinic-barotropic continuum [*Nidzieko et al.*, 2009], which defines the overall evolution of the secondary circulation. This is readily visualized by means of a three-dimensional analysis of the flow field of a branch of the channel. The evolution of the baroclinic-centrifugal equilibrium of the saline underflow as it travels along the 2.5° inclined sinuous channel is inferred from Figure 16. The planes depicted in Figures 16a–16f are defined by the portion of the flow comprised within the isopycnal corresponding to 2.5% of the initial concentration, thus precisely representing the saline underflow, alone. The sloshing of the stratified saline flow as it bumps against the walls of the channel and folds at the apex of the first bend is manifest in Figure 16g. When the saline leaves the straight section of the channel and enters the bend (Figure 16a), the tilting of the isopycnals is mild, while centrifugal acceleration immediately becomes predominant (Figure 16a). The sense of rotation is clearly river-reversed. The outward pushing component of the flow transports salt toward the outer side of the bank, intensifying the tilting of the isopycnals and setting up the conditions for the magnification of the baroclinic pressure gradient. In Figure 16b the saline is leaving the first curve and approaches

the first inflection of the bend. The departure from the curvature-dominated region of the channel is apparent from the weakening of the centrifugal force and the growth of the return flow located at the upper portion of the plane as a result of baroclinic forcing. The baroclinic pressure gradient becomes the dominant term as the curvature effect vanishes. Halfway through the straight section of the channel (Figure 16c), the isopycnals are tilted both at the bottom left and at the upper right side of the channel. This pattern of stratification produces a baroclinic circulation which drives a bottom current from the left side to the right side of the channel and a strong cell of clockwise circulation at the upper right side of the plane. A better structured pattern of circulation is found far from the upstream and downstream region of curvature (Figure 16d). At the plane located close to the first inflection point of the bend, isopycnals are mildly tilted against the outer bank (right side of the channel in Figure 16) in the upper part of the channel and against the inner bank at the bottom right side of the channel. Given the very low influence of centrifugal acceleration at this location, the transverse flow is mainly driven by baroclinic forcing and advective redistribution of momentum. At the bottom, the baroclinic pressure gradient is directed toward the right side of the channel, which is now the outer bank. This implies that at the time the flow approaches the region of more pronounced curvature, baroclinic pressure gradients and centrifugal force can act in concert with one another (see the bottom right side of the plane in Figure 16d). As the flow travels closer to the apex of the bend, the centrifugal force quickly grows in intensity and the salt mixture is pushed against the outer bank, tilting the isopycnals (Figure 16e). The centrifugal and baroclinic force are once again opposed to each other. When the saline approaches the apex of the first bend, the centrifugal acceleration has gained sufficient intensity to overshadow the baroclinic pressure gradient. The secondary circulation, at this stage, is curvature dominated and river-reversed.

[51] It is estimated that the timescale required for the cross-stream baroclinic pressure gradient to adjust to the centrifugal forcing varies from about 16 sec at an axial slope of 0.43° to 11 sec at 1.5° to 9 sec at 2.5°. Conversely, the timescale for the flow to travel around the bend from the inflection upstream of the first bend apex to the inflection downstream of the same bend is approximately 12, 8 and 7 sec for the 0.43°, 1.5° and 2.5° cases, respectively. This suggests that baroclinically induced flow may not have fully developed at the bend apex, however, when the baroclinic forcing is compared to the centrifugal term, its role in determining the reversed flow cell becomes apparent. The relative importance of the centrifugal and baroclinic terms for the two cases with 0.43° and 2.5° axial slope is estimated in Figure 17. The baroclinic forcing, Figures 17a and 17d, closely resembles the distribution of crosswise density gradients. At 0.43°, Figure 17a, the baroclinic pressure gradient faintly opposes the centrifugal acceleration. The overall cross-stream forcing for the 0.43° case, Figure 17c, computed by subtracting the baroclinic term from the centrifugal term, confirms that the flow is primarily controlled by the centrifugal acceleration. At 2.5°, Figure 17f, the centrifugal term controls the flow below the channel height, while the baroclinically induced flow, despite not fully developed, drives the inward directed return flow at the depth of the shear layer, thus participating in determining the river-reversed cross-stream circulation.

7. Discussion

7.1. Three-Dimensional Flow: Transverse and Longitudinal Coupling

[52] A correlation between the pattern of cross-stream velocity and the vertical position of the maximum downstream velocity was postulated by *Corney et al.* [2006, 2008] and suggested by experimental evidence in *Nidzieko et al.* [2009]. *Keevil et al.* [2007] also suggested that the decrease in height of the downstream velocity maximum along the midchannel axis profile is, in fact, an expression of the three dimensional displacement of the downstream velocity maximum. Therefore, the spatial modification of the downstream velocity as axial slope increases is examined hereafter.

[53] The following can be drawn from the previous observations. First, a connection seems to exist between the location of the core of downstream velocity and the position of the anticlockwise rotating cell, which changes position crosswise along the levee height as a consequence of axial slope modification. When the inclination is increased, the crosswise eddy moves outward (Figures 14b and 14c), and so does the core of the downstream velocity underneath it (Figures 13b and 13c). In the meanwhile the vortex expands, entraining more fluid which, in turn, starts rotating anticlockwise. The growth in the portion of the channel subject to the anticlockwise rotation of the fluid forces the core of downstream velocity down to the basal region of the channel (Figure 13c). This mechanism explains the two-dimensional displacement of the core of the downstream velocity across the bend cross section.

[54] The three-layer structure observed by *Nidzieko et al.* [2009] at the Elkhorn Slough channel provides a clear explanation of the correlation between secondary circulation and the position of the velocity maximum. In the curvature-dominated flow, the peak of centrifugal force arises from the location of the velocity maximum. In the Elkhorn Slough channel, the velocity maximum located at midwater depth gave rise to an outward traveling flow at middepth and associated return flow above and below this, thus generating the three-layer circulation. The same relationship between secondary circulation and the velocity maximum position was found in *Lacy and Monismith* [2001], when the association of dominant centrifugal force and nonlogarithmic downstream velocity profiles with the velocity maximum located deep in the water column gave rise to river-reversed secondary circulation during flood tide.

7.2. Three-Dimensional Flow: Process Mechanics

[55] Density currents traveling along curved channels are essentially regulated by centrifugal acceleration, baroclinic pressure gradient and viscous stresses. The strong density gradients give rise to a significant stratification which, on one hand, is responsible for the onset of baroclinic forcing, but, most importantly, it supports the development of enhanced vertical shear of the streamwise velocity [*Geyer*, 1993]. The centrifugal term is, in turn, heightened by the effect of the stratification. Centrifugal force outbalances the baroclinic forcing and eventually becomes the leading term in regulating

Table 1. Froude Numbers for the Three Experiments at Axial Slopes of 0.43°, 1.5°, and 2.5° at Increasing Distance From the Flow Inlet

Axial Slope	Inlet	Bend 1	Bend 2	Bend 3
0.43°	1.19	0.64	0.62	0.7
1.5°	1.19	0.92	0.85	0.84
2.5°	1.19	1.1	0.82	0.94

the secondary circulation of density driven flows in curved channels. Local equilibrium and a stationary condition is established because of the growth of frictional terms which act against the centrifugal force [*Chant*, 2002]. The key point for interpreting the patterns of secondary circulation lies in the assumption that, in curvature dominated regimes, the outward traveling cross-stream always develops from where the core of the downstream velocity is located.

[56] In Figure 13a, the downstream velocity core occurs at a considerable distance from the channel bed. The height above the bed where the core of downstream velocity is found coincides with the region from which the main, outward traveling cross-stream develops. The main cross-stream flow appears to develop from a region of the channel cross section close to the inner bank and detached from the ground, and from this region it travels outward maintaining the same depth across the entire bend width. Once the crosswise stream of saline collides into the outer bank, it sinks to the bottom and generates the well known clockwise rotating, river-like cell. However, in Figure 13c, the core of the downstream velocity occurs at the bottom of the channel and from this location the main crosswise, outward traveling flow departs. This inner to outer bank flow travels along the channel bed and preserves its original depth until it encounters the sidewall of the channel. When it collides with the outer bank, the basal flow is forced to climb the channel levee, as documented in *Straub et al.* [2008] and *Islam et al.* [2008]. The baroclinic pressure gradient generated by the tilting of the isopycnals due to the effect of the centrifugal force then comes into play, by providing the return flow from the outer to the inner side of the channel. Altogether this gives rise to the anticlockwise, river-reversed secondary flow cell. This observation confirms and reinforces the existing hypothesis concerning the mechanisms which relate the position of the maximum downstream component of velocity with the pattern of secondary circulation.

7.3. Implications for Flow Evolution and Sedimentation

[57] The recognition that both river-like and river-reversed secondary circulation can occur, dependent on the exact properties of the flow, raises some key questions about how the three-dimensional flow field in sinuous submarine channels changes both in space and time. Here we have shown that the height of the velocity maximum in the downstream velocity profile is a key parameter for controlling the nature of the secondary flow, reinforcing the earlier arguments of *Corney et al.* [2008] and *Nidzieko et al.* [2009]. In turn, the position of the velocity maximum is dependent on a number of other controlling factors, such as slope, flow density, and flow stratification. A bulk parameter such as the Froude number reflects some of these terms, but not effects such as flow stratification and resulting changes in velocity profiles. That said, the position of the velocity maximum is positively related to the Froude number, with a marked decrease in the height of U_{max} in supercritical currents compared to subcritical flows [*Garcia*, 1994; *Sequeiros et al.*, 2010]. It is interesting to note, however, that the transition between river-like and river-reversed secondary circulation does not necessarily take place at the supercritical/subcritical boundary, at least for the conditions modeled, but instead occurs at Froude numbers below 1 (see Table 1 and Figure 15).

[58] While knowledge of how these individual and bulk parameters affect the three-dimensional flow dynamics is largely unknown, the present study does provide an outline. Submarine channels on relatively steep slopes, with comparatively high densities, high sediment stratification and therefore higher Froude numbers will likely show reversed secondary circulation. Since slope angles, flow thicknesses, sediment concentration and therefore Froude number typically decrease downstream [*Pirmez and Imran*, 2003] then such flows should see a progressive increase in the position of the velocity maximum away from the bed and therefore should at some point undergo a change in the orientation of secondary flow [*Corney et al.*, 2008]. Furthermore, as such flows wane, or in the case of hyperpycnal flows wax and then wane [*Mulder and Alexander*, 2001], perhaps repeatedly [*Lamb and Mohrig*, 2009; *Lamb et al.*, 2010], the position of this transformation should migrate progressively upstream (waning flow) or downstream (waxing flow). In conjunction with the secondary flow changes, the position of the downstream velocity core can also be expected to migrate both outward (waxing flow) and inward(waning flow).

[59] It is unclear exactly what effect such transformation in secondary flow orientation and associated movement of the downstream velocity core may have on sedimentation and channel evolution. What has been shown in previous studies is that river-reversed secondary flows produce (1) enhanced overbank sedimentation on outer channel bends [*Keevil et al.*, 2006] promoting features such as overbank splays [*Dutton et al.*, 2003] and (2) changes in the longitudinal position and grain size patterns of point bars [*Peakall et al.*, 2007a; *Amos et al.*, 2010]. The effects of lateral migration of the velocity core are unknown in submarine channels, but inward shift of the velocity core in tight river bends is known to promote higher velocities over, and erosion of, point bars [*Hickin*, 1978; *Nanson*, 2010]. Such changes may have potential to explain observations of periodic erosion and accumulation in lateral accretion packages [*Abreu et al.*, 2003], though any such linkage would require further studies. What is clearer is that given the known differences in deposits with river-like and river-reversed secondary circulation, then any spatial and temporal variation in the nature of the secondary flow field is likely to produce variations in intrachannel deposits as a function of longitudinal channel position.

8. Conclusion

[60] The results obtained from a series of numerical simulations have been presented in order to clarify the contradiction between previous experimental and numerical results concerning the orientation of the secondary circulation in submerged, sinuous channels.

[61] A numerical model was recursively employed for simulating the flow pattern of a saline density current traveling across a sinuous channel constrained by vertical sidewalls at four different values of the axial slope. The planform of the geometry, the physical and the numerical specifications and the boundary conditions are as similar as possible to those prescribed by *Imran et al.* [2004] and *Kassem and Imran* [2004]. The key difference being in the near-wall modeling approach employed here for capturing, with an improved accuracy, the bottom boundary solution.

[62] The first set of results achieved with axial slopes of 0.08° and 0.43° very strongly match the earlier numerical and experimental observations of *Kassem and Imran* [2004] and *Imran et al.* [2007]. The present results confirm the occurrence of a river-like secondary circulation at the first channel bend of the sinuous channel where a clockwise circulation, for a downstream observer, is predicted.

[63] Tests performed at axial slopes of 1.5° and 2.5° for the same model reveal the onset of a transitional stage followed by the complete overturning of the initial mode of secondary circulation. Once the steady state is reached for the case with the axial slope of 2.5°, a river-reversed pattern of secondary circulation may be observed where an anticlockwise rotation, for an observer downstream of the bend, controls the whole cross-stream flow pattern.

[64] Drawing inspiration from the existing work on tidal processes, submarine channels are assimilated to systems where curvature, stratification and friction represent the leading terms. Coriolis force does indeed play a role, but this term is neglected in this study. The advective displacement of the transported specie (taken to be salt, in this study) generates important baroclinic pressure gradients and regions with intense stratification. The baroclinic pressure gradients operate in order to annihilate the density differences and, by doing so, they mainly act against the centrifugal force. The effect of the baroclinic forcing becomes apparent when the centrifugal force weakens and the saline flow sloshes against the lateral side of the channel. The stratification associated with the density current, on the other hand, provides an additional source of vertical shear to the streamwise component of velocity. This role of the stratification is determinant in further enhancing the strength of the centrifugal acceleration which, in general, is responsible for controlling the main component of the transverse circulation. Because the transverse circulation depends on the centrifugal term and this, in turn, is associated with the velocity maximum, then it becomes apparent that the cross-stream circulation develops from the core of maximum downstream velocity. Provided this, two possible scenarios are predicted. When the velocity maximum is high above the bed, as occurs for low inclinations of the axial slope as well as for weak stratification, the lateral flow travels toward the outer bank where it either sinks, as in Figure 14a, generating a river-like circulation, or splits in two branches, as in Figure 14b. When the velocity maximum is close to the bed, as occurs, in this study, when a higher inclination is accounted for, or in the case of a stronger stratification, then the lateral flow remains close to the bed as it travels toward the outer bank. As the flow encounters the outer sidewall of the channel it rises and generates a river-reversed secondary circulation.

[65] These results bring evidence that the earlier findings which respectively supported the occurrence of the river-like or river-reversed secondary circulation are not mutually exclusive. On the contrary, it is confirmed here that, as it is observed in estuarine systems, a transition from one mode to the other is indeed feasible and can be easily achieved by means of a mild alteration of the axial slope.

[66] As a result of decreasing slope angles or changes in other flow properties such as sediment concentration and flow thickness decreasing downstream many flows can be expected to exhibit a transition between river-like and river-reversed secondary behavior and associated lateral migration of the downstream velocity core. Given these spatial variations in helical flow then there are also likely to be longitudinal variations in the nature of sedimentary deposits.

[67] The present analysis, following the previous experimental and numerical studies, utilized a crude approximation where the fluid dynamics of a turbidity current were assimilated to those of a laboratory scale saline flow. In order to be representative of real scale turbidity currents, scaling up of the model would be beneficial. However, in order to do so a significant increase in computational effort is needed if very high Reynolds numbers are to be accounted for along with a suitable treatment of the near-wall dynamics. In addition, given the importance that the position of the core of the downstream velocity has on the whole cross-stream circulation, the mild stratification typical of a saline gravity current may in many ways turn out to be only partially representative of what could occur in a strongly stratified sediment-laden gravity current. In the latter, the steep vertical gradient of sediment concentration could well be associated with a corresponding steep vertical velocity gradient and thus with reinforced centrifugal forcing. In this case, the core of downstream velocity would be even more likely to be close to the channel bed, thus facilitating the onset of the river-reversed circulation mode.

[68] **Acknowledgments.** The lead author thanks the EU for the award of an Early Stage Training Marie Curie Fellowship grant.

References

Abreu, V., M. Sullivan, C. Pirmez, and D. Mohrig (2003), Lateral accretion packages (LAPs): An important reservoir element in deep water sinuous channels, *Mar. Pet. Geol.*, *20*, 631–648.

Amos, K., J. Peakall, P. W. Bradbury, M. Roberts, G. Keevil, and S. Gupta (2010), The influence of bend amplitude and planform morphology on flow and sedimentation in submarine channels, *Mar. Pet. Geol.*, *27*, 1431–1447.

Ashmore, P. E. (1982), Laboratory modelling of gravel braided stream morphology, *Earth Surf. Processes Landforms*, *7*, 201–225.

Babonneau, N., B. Savoye, M. Cremer, and B. Klein (2002), Morphology and architecture of the present canyon and channel system of the Zaire deep-sea fan, *Mar. Pet. Geol.*, *19*, 445–467.

Best, J. L., R. A. Kostaschuk, J. Peakall, P. V. Villard, and M. Franklin (2005), Whole flow field dynamics and velocity pulsing within natural sediment-laden underflows, *Geology*, *33*, 765–768.

Chant, R. J. (2002), Secondary circulation in a region of flow curvature: Relationship with tidal forcing and river discharge, *J. Geophys. Res.*, *107*(C9), 3131, doi:10.1029/2001JC001082.

Chant, R. J., and R. E. Wilson (1997), Secondary circulation in a highly stratified estuary, *J. Geophys. Res.*, *102*, 23,207–23,215.

Chen, H. C., and V. C. Patel (1988), Near-wall turbulence models for complex flows including separation, *AIAA J.*, *26*, 641–648.

Cheng, P., R. E. Wilson, R. J. Chant, D. C. Fugate, and R. D. Flood (2009), Modeling influence of stratification on lateral circulation in a stratified estuary, *J. Phys. Oceanogr.*, *39*, 2324–2337.

Chough, S. K., and R. Hesse (1980), The North-West Atlantic Mid-Ocean Channel of the Labrador Sea: III. Head spill vs. body spill deposits from turbidity currents on natural levees, *J. Sediment. Petrol.*, *50*, 227–234.

Clark, J. D., and K. T. Pickering (1996), *Submarine Channels: Process and Architecture*, 231 pp., Vallis, London.

Clark, J. D., N. H. Kenyon, and K. T. Pickering (1992), Quantitative analysis of the geometry of submarine channels: Implications for the classification of submarine fans, *Geology*, *20*, 633–636.

Corney, R. T. (2005), Numerical, analytical and experimental modelling of channelised gravity currents, Ph.D. thesis, 333 pp., University of Leeds, Leeds, U. K.

Corney, R. K. T., J. Peakall, D. Parsons, L. Elliott, K. J. Amos, J. L. Best, G. M. Keevil, and D. B. Ingham (2006), The orientation of helical flow in curved channels, *Sedimentology*, *53*, 249–257.

Corney, R. K. T., J. Peakall, D. Parsons, L. Elliott, J. L. Best, R. E. Thomas, G. M. Keevil, D. B. Ingham, and K. J. Amos (2008), Reply to discussion of Imran et al. on "The orientation of helical flow in curved channel" by Corney et al., *Sedimentology*, *55*, 241–247.

Dutton, S. P., W. A. Flanders, and M. D. Barton (2003), Reservoir characterization of a Permian deep-water sandstone, East Ford field, Delaware Basin, Texas, *AAPG Bull.*, *87*, 609–627.

Eaton, B. C., and M. Church (2004), A graded stream response relation for bed load dominated streams, *J. Geophys. Res.*, *109*, F03011, doi:10.1029/2003JF000062.

Garcia, M. (1994), Depositional turbidity currents with poorly sorted sediment, *J. Hydraul. Eng.*, *120*, 1240–1263.

Geyer, W. R. (1993), Three-dimensional tidal flow around headlands, *J. Geophys. Res.*, *98*, 955–966.

Hampton, M. A. (1972), The role of subaqueous debris flow in generating turbidity currents, *J. Sediment. Petrol.*, *42*, 775–793.

Heindel, T. J., S. Ramadhyani, and F. P. Incropera (1994), Assessment of turbulence models for natural convection in an enclosure, *Numer. Heat Transfer, Part B, Fundamentals*, *26*, 147–172.

Henkes, R. A. W. M., F. F. Van Der Vlugt, and C. J. Hoogendoorn (1991), Natural-convection flow in a square cavity calculated with low-Reynolds-number turbulence models, *Int. J. Heat Mass Transfer*, *34*, 377–388.

Hickin, E. J. (1978), Mean flow structure in meanders of the Squamish River, British Columbia, *Can. J. Earth Sci.*, *15*, 1833–1849.

Ikeda, S., and T. Nishimura (1986), Flow and bed profile in meandering sand-silt rivers, *J. Hydraul. Eng.*, *112*, 562–579.

Imran, J., G. Parker, and C. Pirmez (1999), A nonlinear model of flow in meandering submarine and subaerial channels, *J. Fluid Mech.*, *400*, 295–331.

Imran, J., A. Kassem, and S. M. Khan (2004), Three-dimensional modeling of density current I. Flow in straight confined and unconfined channels, *J. Hydraul. Res.*, *42*, 578–590.

Imran, J., M. Islam, H. Huang, A. Kassem, J. Dickerson, C. Pirmez, and G. Parker (2007), Helical flow couplets in submarine gravity underflows, *Geology*, *113*, 917–926.

Imran, J., A. M. Islam, and A. Kassem (2008), Discussion of "The orientation of helical flow in curved channels" by Corney et al., *Sedimentology*, *55*, 235–239.

Islam, A. M., and J. Imran (2008), Experimental modeling of gravity underflow in a sinuous submerged channel, *J. Geophys. Res.*, *113*, C07041, doi:10.1029/2007JC004292.

Islam, A. M., J. Imran, C. Pirmez, and A. Cantelli (2008), Flow splitting modifies the helical motion in submarine channels, *Geophys. Res. Lett.*, *35*, L22603, doi:10.1029/2008GL034995.

Kader, B. (1981), Temperature and concentration profiles in fully turbulent boundary layers, *Int. J. Heat Mass Transfer*, *24*, 1541–1544.

Kane, I. A., W. D. McCaffrey, and J. Peakall (2008), Controls on sinuosity evolution within submarine channels, *Geology*, *36*, 287–290, doi:10.1130/G24588A.1.

Kassem, A., and J. Imran (2004), Three-dimensional modeling of density current II. Flow in sinuous confined and unconfined channels, *J. Hydraul. Eng.*, *42*, 511–602.

Keevil, G. M., J. Peakall, J. L. Best, and K. J. Amos (2006), Flow structure in sinuous submarine channels: Velocity and turbulence structure in an experimental submarine channel, *Mar. Geol.*, *229*, 241–257.

Keevil, G. M., J. Peakall, and J. M. Best (2007), The influence of scale, slope and channel geometry on the flow dynamics of submarine channels, *Mar. Pet. Geol.*, *24*, 487–503.

Khripounoff, A., A. Vangriesheim, N. Babonneau, P. Crassous, B. Dennielou, and B. Savoye (2003), Direct observation of intense turbidity current activity in the Zaire submarine valley at 4000 m water depth, *Mar. Geol.*, *194*, 151–158.

Kikkawa, H., S. Ikeda, A. Kitagawa, and C. R. Thorne (1976), Flow and bed topography in curved open channels, *J. Hydraul. Div.*, *102*, 1327–1342.

Klaucke, I., and R. Hesse (1996), Fluvial features in the deep sea: new insights from the glaciogenic submarine drainage system of the Northern Atlantic Mid-Ocean channel in the Labrador Sea, *Sediment. Geol.*, *106*, 223–234.

Kolla, V., H. W. Posamentier, and L. J. Wood (2007), Deep-water and fluvial sinuous channels. Characteristics, similarities and dissimilarities, and modes of formation, *Mar. Pet. Geol.*, *24*, 388–405.

Lacy, J. R., and S. G. Monismith (2001), Secondary currents in a curved, stratified, estuarine channel, *J. Geophys. Res.*, *106*, 31,283–31,302.

Lamb, M. P., and D. Mohrig (2009), Do hyperpycnal-flow deposits record river-flood dynamics?, *Geology*, *37*, 1067–1070.

Lamb, M. P., B. McElroy, B. Kopriva, J. Shaw, and D. Mohrig (2010), Linking river-flood dynamics to hyperpycnal-plume deposits: Experiments, theory, and geological implications, *Geol. Soc. Am. Bull.*, *122*, 1389–1400.

Launder, B. E., and D. B. Spalding (1974), The numerical computation of turbulent flows, *Comput. Methods Appl. Mech. Eng.*, *3*, 269–289.

Middleton, G. V. (1966), Experiments on density and turbidity currents II. Uniform flow of density currents, *Can. J. Earth Sci.*, *3*, 627–637.

Middleton, G. V. (1993), Sediment deposition from turbidity currents, *Annu. Rev. Earth Planet. Sci.*, *21*, 89–114.

Mohrig, D., and I. G. Marr (2003), Constraining the efficiency of turbidity current generation from submarine debris flows and slides using laboratory experiments, *Mar. Pet. Geol.*, *20*, 883–899.

Moreton, D. J., P. J. Ashworth, and J. L. Best (2002), The physical scale modelling of braided alluvial architecture and estimation of subsurface permeability, *Basin Res.*, *14*, 265–285.

Mulder, T., and J. Alexander (2001), The physical character of subaqueous sedimentary density flows and their deposits, *Sedimentology*, *48*, 269–299.

Nanson, R. A. (2010), Flow fields in tightly curving meander bends of low width-depth ratio, *Earth Surf. Processes Landforms*, *35*, 119–135.

Nidzieko, N. J., J. L. Hensh, and S. G. Monismith (2009), Lateral circulation in well-mixed and stratified estuarine flows with curvature, *J. Phys. Oceanogr.*, *39*, 831–851.

Paola, C., K. Straub, D. Mohrig, and L. Reinhardt (2009), The "unreasonable effectiveness" of stratigraphic and geomorphic experiments, *Earth Sci. Rev.*, *97*, 1–43.

Parsons, D. R., J. Peakall, A. E. Aksu, R. D. Flood, R. N. Hiscott, S. Besiktepe, and D. Mouland (2010), Gravity-driven flow in a submarine channel bend: Direct field evidence of helical flow reversal., *Geology*, *38*, 1063–1066.

Paull, C. K., W. Ussler, H. G. Greene, R. Keaten, P. Mitts, and J. Barry (2003), Caught in the act: The 20 December 2001 gravity flow event in Monterey Canyon, *Geo Mar. Lett.*, *22*, 227–232.

Peakall, J., P. Ashworth, and J. Best, J. (1996), Physical modelling in fluvial geomorphology: Principles, applications and unresolved issues, in *The Scientific Nature of Geomorphology*, edited by B. L. Rhoads and C. E. Thorn, pp. 221–253, John Wiley, Chichester, N. Y.

Peakall, J., W. D. McCaffrey, and B. C. Kneller (2000), A process model for the evolution, morphology and architecture of sinuous submarine channels, *J. Sediment. Res.*, *70*, 434–448.

Peakall, J., K. J. Amos, G. M. Keevil, P. W. Bradbury, and S. Gupta (2007a), Flow processes and sedimentation in submarine channel bends, *Mar. Pet. Geol.*, *24*, 470–486.

Peakall, J., P. J. Ashworth, and J. L. Best (2007b), Meander-bend evolution, alluvial architecture, and the role of cohesion in sinuous river channels: A flume study, *J. Sediment. Res.*, *77*, 197–212.

Pirmez, C., and R. D. Flood (1995), Morphology and structure of Amazon Channel, *Proc. Ocean Drill. Program Initial Rep.*, *155*, 23–45.

Pirmez, C., and J. Imran (2003), Reconstruction of turbidity currents in Amazon Channel, *Mar. Pet. Geol.*, *20*, 823–849.

Schlichting, H. (1968), *Boundary Layer Theory*, McGraw-Hill, New York.

Schumm, S. A., M. P. Mosley, and W. E. Weaver (1987), *Experimental Fluvial Geomorphology*, 413 pp., John Wiley, New York.

Seim, H. E., and M. C. Gregg (1997), The importance of aspiration and channel curvature in producing strong vertical mixing over a sill, *J. Geophys. Res.*, *102*, 3451–3472.

Sequeiros, O. E., S. Benoit, R. T. Beaboef, T. Sun, M. H. Garcia, and G. Parker (2010), Characteristics of velocity and excess density profiles of saline underflows and turbidity currents flowing over a mobile bed, *J. Hydraul. Eng.*, *136*, 412–433.

Straub, K. M., D. Mohrig, B. McElroy, J. Buttles, and C. Pirmez (2008), Interactions between turbidity currents and topography in aggrading

sinuous submarine channels: A laboratory study, *Geol. Soc. Am. Bull.*, *120*, 368–385.

Vangriesheim, A., A. Khripounoff, and P. Crassous (2009), Turbidity events observed in situ along the Congo Submarine Channel, *Deep Sea Res., Part II*, *56*, 2208–2222.

Wolfstein, M. (1969), The velocity and temperature distribution of one-dimensional flow with turbulence augmentation and pressure gradient, *Int. J. Heat Mass Transfer*, *12*, 301–318.

Wynn, R. B., B. T. Cronin, and J. Peakall (2007), Sinuous deep-water channels: Genesis, geometry and architecture, *Mar. Pet. Geol.*, *24*, 341–387.

Xu, J. P., M. A. Noble, and L. K. Rosenfeld (2004), In-situ measurements of velocity structure within turbidity currents, *Geophys. Res. Lett.*, *31*, L09311, doi:10.1029/2004GL019718.

Zeng, J., D. R. Lowe, D. B. Prior, W. J. Wiseman, and B. D. Bornhold (1991), Flow properties of turbidity currents in Bute Inlet, British Columbia, *Sedimentology*, *38*, 975–996.

Zhang, L., Y. An, Z. Li, G. Q. Chen, and J. H. W. Lee (2001), Numerical anatomy of lock-release gravity currents, *Commun. Nonlinear Sci. Numer. Simulat.*, *6*, 183–192.

A. D. Burns, F. Giorgio Serchi, and D. B. Ingham, School of Process Material and Environmental Engineering, CFD Centre, University of Leeds, Leeds LS2 9JT, UK. (pmfgs@leeds.ac.uk)

J. Peakall, School of Earth and Environment, Department of Earth Sciences, University of Leeds, Leeds LS2 9JT, UK.